# ABSTRACT

Title of dissertation: GRAPHENE CHEMICAL-VAPOR-DEPOSITED ON PLATINUM: SYNTHESIS, CHARACTERIZATION AND MAGNETO-TRANSPORT PROPERTIES
Jinglei Ping, Doctor of Philosophy, 2013

Dissertation directed by: Professor Michael Sears Fuhrer
Department of Physics

Graphene with large grain size and high electronic mobility was synthesized by ambient-pressure chemical vapor deposition on platinum and transferred to a variety of substrates for characterization by electrical transport, Raman spectroscopy, and transmission electron microscopy. The grain boundaries and pyramid-like multilayer structures of graphene samples prepared in this way were imaged with dark-field transmission electron microscopy, and a method was developed to use differences in first- and second-order diffraction intensities to characterize the layer-number and stacking-order of graphene up to at least seven layers. Combining this dark-field method with secondary electron microscopy, electron backscatter diffraction, Raman microscopy, and electronic transport measurements, it was also discovered that nano-crystalline carbon impurities distributed inhomogeneously under mono-layer graphene. These impurities were distributed inhomogenously, exhibiting micron-sized islands of denser impurity concentration whose shapes depended on the orientation of the grains of the Pt substrate. In such impurity-decorated samples both

linear and quadratic magnetoresistance was observed. The linear magnetoresistance was found for carrier densities well beyond filling the ground Landau level, therefore Abrikosov's quantum magnetoreistance is ruled out. Sample 1, 2, and 3 with suppressing inhomogeneity were synthesized by controlling growing conditions in the chemical vapor deposition process. The magnetoresistance positively correlates with the density of inhomogeneity. The magnetoresistance in samples with widely varying impurity concentrations can be described by a unique function of the ratio of carrier-density inhomogeneity to gate-induced carrier density, and can therefore be attributed to impurity-induced inhomogeneity.

# GRAPHENE CHEMICAL-VAPOR-DEPOSITED ON PLATINUM: SYNTHESIS, CHARACTERIZATION AND MAGNETO-TRANSPORT PROPERTIES

by

Jinglei Ping

Dissertation submitted to the Faculty of the Graduate School of the
University of Maryland, College Park in partial fulfillment
of the requirements for the degree of
Doctor of Philosophy
2013

Advisory Committee:
Professor Michael Fuhrer, Chair/Advisor
Professor John Cumings
Professor Michael Fisher
Professor Min Ouyang
Professor Ellen Williams

# Dedication

To Buqing.

# Acknowledgments

First and foremost I would like to thank my advisor, Professor Michael Sears Fuhrer. I would like to thank him for his instruction, encouragement and patience. I benefit a lot from Michael characteristic way of carrying out research: building simple physical pictures, telling straightforward stories and criticizing. As a constructive and independently-minded physicist, Michael is also an advisor together with whom I was working on the experiment, cleaning the lab, and enjoying wonderful beer breaking. In Fuhrer's group I enjoy physics and life and I feel very lucky being a member of it.

I would also like to thank two other professors particularly. Professor Fisher encouraged and inspired me to take a big step after I joined Maryland in 2008. His attitudes towards research and academic are treasures I cherish most. Professor Williams, my first advisor, took good care of me and patiently lead me into the wonderland of surface physics.

People in the condensed matter physics group have given me selfless help and enriched my graduate life. Prof. Einstein is always the first one from whom I seek help when facing theoretical problems. Dr. Cullen is an encyclopaedia of vacuum technology and is always there to give valuable hints. Chuan used his last month in Maryland training me on the cryostat and cheered with me when my first data of quantum Hall effect in graphene was generated. Mahito joined me in the adventure of searching sample under AFM and excellent food as well. Kristen Burson never forgot me every thanksgiving and her aloe gave my family lots of fun.

Michelle Groce is the person I would like to talk with about nice STM images and culture and history. Dohun is really good to have in group to keep the wire-bonding machine healthy. Of course, my companions Jack and Jake, shared the hard but most fantastic time with me in Australia.

There are, of course, Australian fellows in Monash University whom I would like to thank: Prof. Amelia Liu, Dr. Xi-ya Fang and Prof. Matthew Weyland, for the enjoyable and harvest discussions about electron microscopy.

I would like to thank Prof. Michael Coplan and Mrs. Debbie Jenkins who have been giving me selfless help during the past five years.

I owe deepest thanks to my family: my parents, who have their only child living in a country with 12 hours time-zone difference; my wife Rian, with whom I share happiness, excitement, and every experience I have in our everyday adventures. And our unborn daughter Buqing, from whom I received unlimited joy.

Thank you all.

# Preface

Graphene is a one-atom-thick layer of graphite. As an allotrope of carbon, graphene has unique mechanical[1], electronic[2], and optical[3] properties and has been investigated widely as a promising post-silicon electronic material after it was discovered in 2004[4].

Two-dimensional graphene is the only low-dimensional carbon allotrope (others are one-dimensional carbon nanotube and zero-dimensional fullerene) that can be prepared via the top-down method: the well known exfoliation method[4]. However, the application of this method is limited due to small size ($< 100\mu$m) of the samples prepared. Thus the method of chemical vapor deposition (CVD) was developed to produce graphene samples with macroscopic size ($\sim$ m). This method of CVD with platinum as the catalyst and substrate was adopted to synthesize centimeter size monolayer graphene samples with 100 $\mu$m crystal grains[5] as introduced in Chapter 1.

Despite having good electronic properties, the samples synthesized on Pt were found to be decorated with carbon impurities. Chapter 2 describes the development of methods based on selected area electron diffraction (SAED) patterns and dark field (DF) images of transmission electron microscopy (TEM) to characterize layer-number and stacking sequence of graphene up to at least seven layers. Using techniques from Chapter 2 and combining other methods such as Raman microscopy (see Appendix A), secondary electron microscopy (SEM), electron backscatter diffraction (EBSD), energy-dispersive X-ray (EDX), atomic force microscopy (AFM) and high

resolution TEM (HRTEM), the impurities were identified as nanocrystalline carbon layers growing under the continuos monolayer graphene. Such impurities distribute throughout the whole sample inhomogeneously and concentrate in some regions to form optically visible island-like impurities whose morphology depends on the orientation of the substrate as in Chapter 3.

In Chapter 4 I explore the electronic transport properties of such impurity-decorated graphene sample. A linear-to-quadratic transition of magnetoresistance was observed at Landau level filling $\gg 1$ indicating a classical rather than a quantum origin. With Sample 1, 2 and 3 of different density of carbon impurities controlled by growing conditions in the chemical vapor deposition process, the magnetoresistance was found to positively correlate with the inhomogeneity density induced by the carbon impurities. The magnetoresistance was described by a unique function of the ratio of carrier-density inhomogeneity $n^*$ to gate-induced carrier density $n$, and therefore attribute the magnetoresistance to impurity-induced inhomogeneity. It was found that the inhomogeneity has a significant remnant over a large range of carrier density scaled by the inhomogeneity density $n^*$.

Except the introductory chapter, each chapter in this thesis, though logically correlated, tells a relatively independent story and has been either published or submitted or prepared as a single article. I have taken part in the preparation, writing, and revision of all those articles, published or not. Thus I uses similar, and sometimes exactly the same, words in this thesis as those in the manuscripts.

# Table of Contents

# List of Figures

# List of Abbreviations

| | |
|---|---|
| 2D | two dimensional |
| AFM | atomic force microscopy |
| CVD | chemical vapor deposition |
| DF | dark field |
| DP | diffraction pattern |
| EBSD | electron backscattering diffraction |
| EDX | energy dispersive X-ray spectroscopy |
| FE | field effect |
| HRTEM | high-resolution transmission electron microscopy |
| IPF | inverse pole figure |
| MR | magnetoresistance |
| PMMA | Poly(methyl methacrylate) |
| RD | reference direction |
| RMR | reduced magnetoresistance |
| RT | room temperature |
| SAED | selected area electron diffraction |
| sccm | standard cubic centimeter per minute |
| SEM | secondary electron microscopy |
| STEM | scanning transmission electron microscopy |
| STM | scanning tunneling microscopy |
| TEM | transmission electron microscopy |

Chapter 1

# INTRODUCTION

This chapter is an introduction to the aspects of graphene related to this thesis: the crystal structure and band structure, the synthesis of graphene via chemical vapor deposition(CVD), the method of transferring graphene from growth substrate to other substrate, and a summary of the characterization methods employed in the works discussed in this thesis.

## 1.1 Graphene Crystal Structure

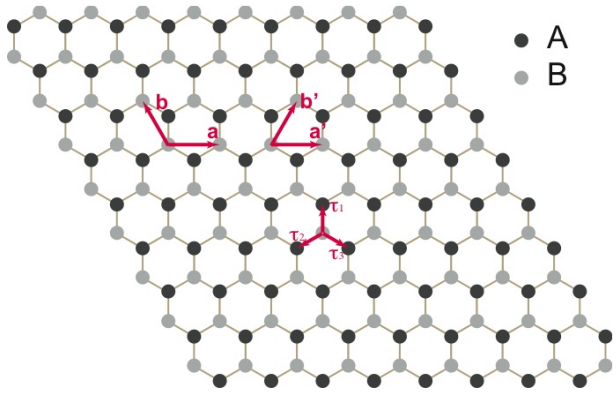


Figure 1.1: Monolayer graphene crystal strucutre. Each unit cell contains two atoms: A and B. The Bravais lattice is triangular.

The structure of graphene's honeycomb lattice is oblique in terms of triangular Bravais lattice, as shown in Figure 1.1. There are two atoms A and B in each unit cell. The primitive vectors are $\mathbf{a} = a(1, 0)$ and $\mathbf{b} = a(-1/2, \sqrt{3}/2)$, where

$a = 0.246$ nm is the lattice constant. Occasionally, $\mathbf{a}' = \mathbf{a} = a(1, 0)$ and $\mathbf{a}'' = a(1/2, \sqrt{3}/2)$ is also adopted. Vectors connecting nearest neighboring carbon atoms are $\tau_1 = a(0, 1/\sqrt{3})$, $\tau_2 = a(-1/2, -1/2\sqrt{3})$, and $\tau_3 = a(1/2, -1/2\sqrt{3})$. A unit cell has an area

$$\Omega_0 = \frac{\sqrt{3}}{2}a^2. \tag{1.1}$$

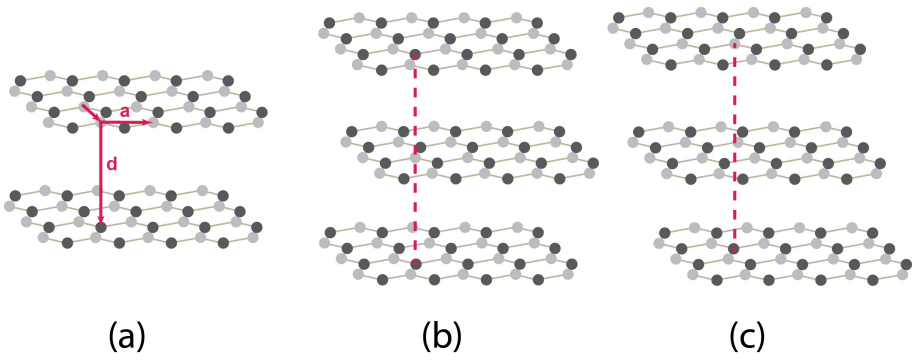


Figure 1.2: Bilayer graphene (a) and trilayer graphene with Bernal (AB) stacking (b) and rhombohedral (ABC) stacking (c).

The concept of layer-number and stacking-order arises when there is more than one layer of graphene. To minimize the free energy, graphene tends to stack closely, which induces a shift of the second added layer with respect to the first one. The layer to layer distance is $d = 0.34$nm, as in Figure 1.2(a). There are two possible stacking modes when adding another layer of graphene to bilayer graphene: Bernal stacking as in Figure 1.2(b), by adding a third layer shifting in the opposite direction of the second layer, and rhombohedral stacking as in Figure 1.2(c), in which case the third layer shifts further in the direction of the second layer. The physical properties of multi-layer graphene depend greatly on the layer-number[7] and stacking-order[8, 9].

## 1.2 Graphene Band Structure

Given the crystal structure of graphene shown in Section 1.1, we can obtain the band structure of graphene via the tight-binding approach[10, 11].

The conducting electrons are in the $\pi$ band, which comes from the $p_z$ orbitals of the carbon atoms. For symmetry reasons, the $\pi$ band can be calculated independently from the $\sigma$ band, which comes from $s$, $p_x$ and $p_y$ orbitals. And since there are two atoms, A and B, in a primitive cell in the graphene lattice, the Hamiltonian matrix [12] in the tight-binding model can be written as:

$$\mathcal{H} = \begin{pmatrix} \mathcal{H}_{AA} & \mathcal{H}_{AB} \\ \mathcal{H}^*_{AB} & \mathcal{H}_{BB} \end{pmatrix}. \tag{1.2}$$

By ignoring integrals between any pair of atoms other than nearest neighbors we have

$$\mathcal{H} = \begin{pmatrix} \epsilon_p & tf(\mathbf{k}) \\ tf^*(\mathbf{k}) & \epsilon_p \end{pmatrix}, \tag{1.3}$$

where $\epsilon_p$ is the atomic electron energy $-\int dV \phi^*(\mathbf{r}) H \phi(\mathbf{r})$ whose value is arbitrarily chosen to be 0 while $t$ is the nearest neighbor integral $-\int dV \phi^*(\mathbf{r}-\mathbf{R}) H \phi(\mathbf{r})$. The term $f(\mathbf{k})$ is the geometric factor

$$\begin{aligned} f(\mathbf{k}) &= \sum_{\delta} e^{i\mathbf{k}\cdot\delta} \\ &= 2e^{-ik_y a/2} \cos\left(\frac{k_x a\sqrt{3}}{2}\right) + e^{ik_y a}. \end{aligned} \tag{1.4}$$

Thus we have the energy

$$E(\mathbf{k}) = \pm t|f(\mathbf{k})| = \pm t\sqrt{3 + s(\mathbf{k})}, \tag{1.5}$$

where

$$s(\mathbf{k}) = 2\cos\left(\sqrt{3}k_x a\right) + 4\cos\left(\frac{\sqrt{3}}{2}k_x a\right)\cos\left(\frac{3}{2}k_y a\right). \tag{1.6}$$

It can be seen that at two symmetrically unequal points $\mathbf{K} = (2\pi/3\sqrt{3}a, -2\pi/3a)$ and $\mathbf{K}' = (-2\pi/3\sqrt{3}a, -2\pi/3a)$, $E(\mathbf{K}) = E(\mathbf{K}') = 0$, meaning that band crosses at $\mathbf{K}$ and $\mathbf{K}'$, the so called Dirac points. The band structure is shown in Figure 1.3(a).

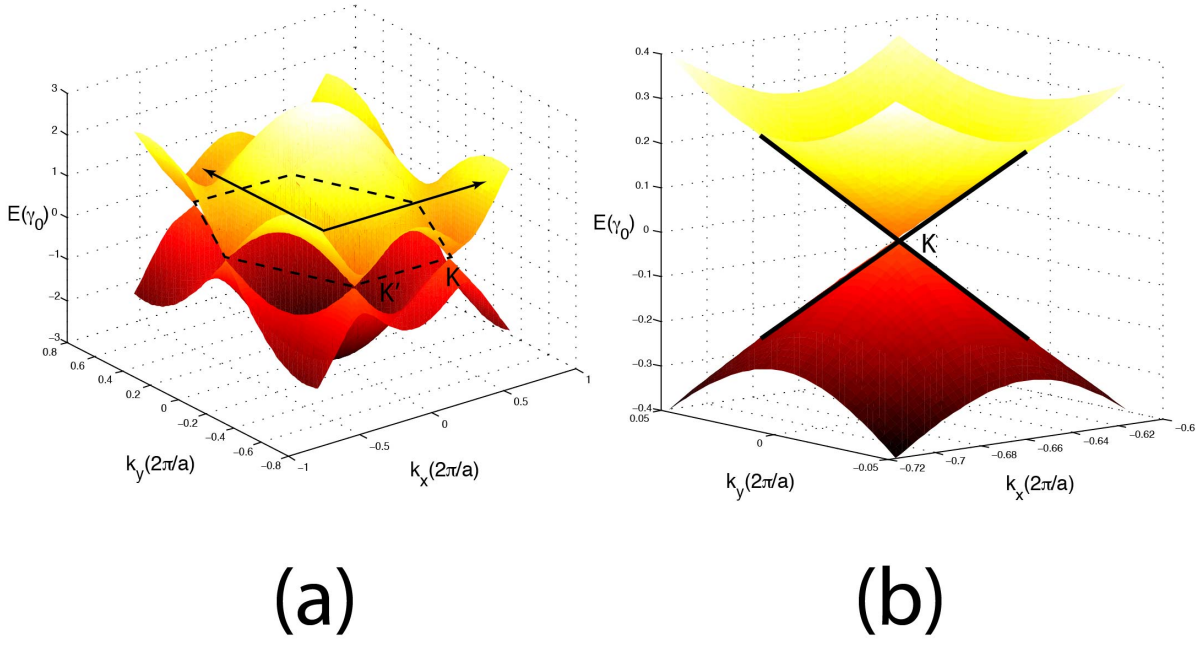


Figure 1.3: Graphene band structure calculated by tight-binding theory. The x and y axes are $k_x a$ and $k_y a$, the z axis represents the scale of energy. In (a) $k_x a$ and $k_y a$ range from $-\pi$ to $\pi$. The maximum and minimum values of the energy in the band structure is $3t$ and $-3t$ respectively. Linear dispersion relationship close to the Dirac point is shown in (b).

In the light of second quantization, the Hamiltonian of Equation 1.3 can also

be written in a suggestive form

$$H = -t \sum_{i,j,\sigma} (a^{\dagger}_{i\sigma} b_{j\sigma} + h.c.) \tag{1.7}$$

where $i$ or $j$ represents orbital of atom on site A or B and $\sigma$ is the spin. The wave function can be written as

$$\begin{pmatrix} \alpha_{\mathbf{k}} \\ \beta_{\mathbf{k}} \end{pmatrix} = \sum_{i} e^{i\mathbf{k}\cdot\mathbf{R}_i} \begin{pmatrix} a^{\dagger}_{i} e^{-i\mathbf{k}\cdot\delta/2} \\ b^{\dagger}_{i} e^{i\mathbf{k}\cdot\delta/2} \end{pmatrix}, \tag{1.8}$$

where $\delta$ is the vector pointing from sublattice A to B. Thus the eigenstate component arising from K and that from K$'$ are decoupled with each other and can be written in a spinor form with component $e^{\pm i\mathbf{k}\cdot\delta/2}$. This quantized quantity called isospin, together with pseudospin arising from unequal sublattice A and B, are two counter quantities to the real spin $\sigma$.

Expanding to first order of Equation 1.5, we can write the Hamiltonians as

$$\mathcal{H}_{K'}(\mathbf{q}) \approx \frac{3at}{2} \begin{pmatrix} 0 & \beta(q_x + iq_y) \\ \beta^*(q_x - iq_y) & 0 \end{pmatrix}, \tag{1.9}$$

and

$$\mathcal{H}_{K}(\mathbf{q}) \approx \frac{3at}{2} \begin{pmatrix} 0 & \beta^*(q_x - iq_y) \\ \beta(q_x + iq_y) & 0 \end{pmatrix}, \tag{1.10}$$

where $\beta = e^{5i\pi/6}$, $\mathbf{q} = \mathbf{k} - \mathbf{K}'$ for $\mathcal{H}_{K'}$ and $\mathbf{q} = \mathbf{k} - \mathbf{K}$ for $\mathcal{H}_{K}$. After combination and unitary transformation[13], we have

$$\mathcal{H}_{K,K'}(\mathbf{q}) = \frac{3at}{2} \begin{pmatrix} 0 & q_x \mp iq_y \\ q_x \pm iq_y & 0 \end{pmatrix}, \tag{1.11}$$

which is linear with respect to $q_x$ and $q_y$, as shown in Figure 1.3(b). Defining $\hbar v_F = 3at/2$, we have the linear dispersion relationship of graphene band structure

close to the Dirac points:

$$E = \pm \hbar v_F q. \tag{1.12}$$

This linear dispersion relationship is analogous to that of massless relativistic particles with momentum $q$. The role of the speed of light is played here by the Fermi velocity $v_F = 3at/2\hbar \approx c/300$. In other words, electrons in graphene have a constant Fermi velocity $v_F$ as the Fermi level changes, which is a property more similar to photons rather than to electrons.

The Hamiltonian in Equation 1.11 can be written as

$$H_{\mathrm{K}} = \hbar v_F \boldsymbol{\sigma} \cdot \mathbf{q}, \tag{1.13}$$

where $\boldsymbol{\sigma}$ is the Pauli matrices, and

$$H_{\mathrm{K}'} = H_{\mathrm{K}}^{\mathrm{T}}. \tag{1.14}$$

## 1.3 Chemical Vapor Deposition of Graphene

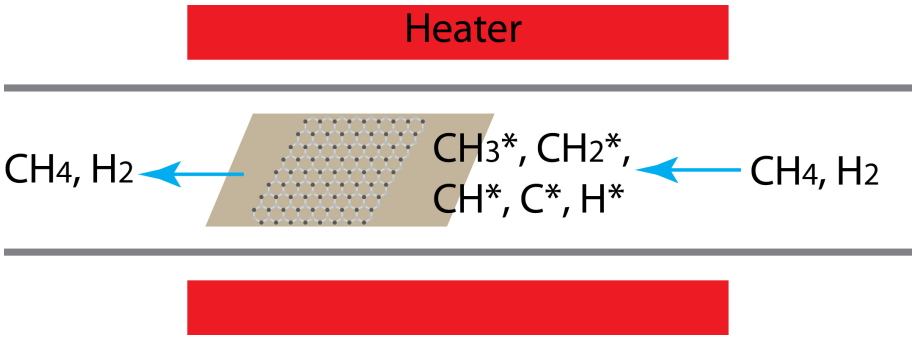


Figure 1.4: Schematic of graphene synthesis process by chemical vapor deposition.

Graphene is the only allotrope of carbon that can be obtained from naturally existing material, graphite, by mechanical exfoliation[4], which is widely used as a

clean and easy way to prepare graphene in the laboratory. As a crucial disadvantage for applications, the size of exfoliated graphene is usually limited to linear dimension below 100$\mu$m. Thus attempts to obtain large-size graphene have never stopped after graphene was discovered. Examples are chemical vapor deposition (CVD)[5, 14, 15] and epitaxial growth from SiC[16]. CVD has the advantages of high yield, low cost, and large size compared to epitaxial growth, making it the most prominent method for industrial production of graphene.

Even though copper is the most widely used catalyst for CVD of graphene, platinum has risen rapidly after its capacity of catalyzing centimeter-scale monolayer graphene at ambient pressure (copper-catalyzed CVD requires a low-pressure furnace), and transfer of graphene from Pt by electrolysis, enabling reuse of substrate, has been reported[5]. The CVD process of graphene on platinum is illustrated in Figure 1.4. A piece of 2 cm $\times$ 1 cm $\times$ 2 $\mu$m platinum foil is placed on a quartz boat in the center heating zone of a quartz tube following with hydrogen($H_2$) gas whose mass flow rate is controlled by a flowcontroller. The boat is then heated up to about 1000° C in one hour. After the temperature is hold for 15 minutes for annealing, methane($CH_4$) gas is turned on during the deposition duration. After the intended amount of graphene has been deposited, the quartz tube is pulled out of the heating zone of the furnace for fast cooling and the methane supply is turned off as the temperature drops below 650° C.

The decomposition process of methane takes place automatically, due to the lowering of free energy from reactants, methane and hydrogen, to the product, graphene. When the temperature increases over 700° C, the speed of methane de-

composition accelerates in the presence of catalyst platinum[5], generating a mixture components of active $CH_3^*$, $CH_2^*$, $CH^*$, and $C^*$. The active $C^*$ deposited on platinum forms graphene. It should be noted that above about 500° C deposited carbon can be etched by hydrogen. Thus the formation of graphene is a complex balancing process of growing and etching and interaction with catalyst[17, 18, 19] in addition to diffusion and segregation[19]. The mechanism of CVD process of graphene remains an open question. And it is not confirmed if the CVD process on copper and on platinum share the same mechanism even though there are clues in our experiment supporting a positive answer to this question.

Thus temperature and mass flow rate of reactants, methane and hydrogen, heating rate and reaction time are adjustable parameters to control the growth of graphene. Low pressure, which is necessary to produce large-size single-crstal graphene in CVD process on copper[15], is not crucial to achieve this on platinum[5]. In all CVD experiment in this thesis, ambient pressure is used.

Technically, the advantages of using platinum as catalyst are summarized:

- The ambient pressure reduces the difficulty to obtain graphene of good quality, making it unnecessary to use the costly equipment for preserving low-pressure at high temperature.
- The platinum foil is reusable. Platinum as an inert metal does not react with most acids or alkalis. Thus electrolysis method is used to "peel" graphene off from the substrate as described in Section 1.4. The graphene sample obtained in this way is much cleaner than that obtained by wet-etching.

- Graphene synthesized on platinum is intrinsically decorated with carbon impurities. Such decoration can be adjusted, from almost none to fully-covered, by adjusting the growing condition such as temperature and mass flow rate of reactants. We found that the magnetoresistance depends sensitively on the carbon impurity coverage and thus can be adjusted as well, as descussed in Chapter 4.

It should be noted that though the grain size of our sample is large($>100\mu$m), graphene produced by CVD is polycrystal. Grain boundaries exist between the junction of each two monocrystal grains. It is also not completely uniform: there are pyramid-like multilayer impurities as discussed in Chapter 2 and more importantly, nanocrystalline graphene impurities as discussed in Chapter 3.

For comparison and investigation purpose, I also grow graphene sample on 25 $\mu$m thick high purity copper foil (99.999%) at 1040° C in an ambient-pressure furnace[15, 20]. The sample is annealed for 30 minutes under flowing 430 sccm (standard cubic centimeter per minute) argon and 170 sccm hydrogen to remove oxide impurities and increase copper grain size. Then 10 sccm methane gas is added for eight minutes and many-layer graphene is deposited. Then the sample is annealed in argon/hydrogen with the same temperature and gas flow rates for 30 minutes and then cooled down. The average number of layers can be controlled by the hydrogen etching duration.

I use a four-step method to transfer synthesized graphene on copper to substrates: (1) two layers of PMMA, Poly(methyl methacrylate) (MicroChemCorp

PMMA 950 A4) are spin coated onto graphene with speed of 6000 rpm for 45 seconds; (2) the coated sample is immersed in CE-100 (Transene) copper etchant for 5 minutes and rinsed in de-ionized water so that graphene on the uncovered side of the copper foil is removed; (3) the sample is immersed in CE-100 at room temperature for sufficient time so that only PMMA and attached graphene is left; (4) the PMMA with attached graphene is rinsed in de-ionized water and then transferred to a silicon dioxide wafer or a silicon transmission electron microscopy (TEM) sample holder with a 1.0 mm x 1.0 mm window covered by 50 nm thick silicon nitride membrane. To remove PMMA, samples are annealed for four hours at 400° C under flowing argon (300 sccm) and hydrogen (700 sccm). No noticeable changes are observed by secondary electron microscopy (SEM) for graphene single-crystal flakes annealed at the same condition, indicating that no additional etching takes place during the 400° C anneal.

## 1.4 Electrolysis Transferring Method

Wet-etching is widely used to transfer graphene synthesized on copper. For the reason of (i) expensiveness of platinum and (ii) cleanness, an electrolysis method is adopted to transfer graphene synthesized on platinum[5]. A layer of PMMA is spin coated onto graphene on platinum foil with speed of 2000 rpm. The graphene-PMMA-coated platinum is then connected with the cathode of a current supplier, as in Figure 1.5, and to the anode, a piece of bare platinum is connected. Then both foils are immersed in a 1 M sodium hydroxide solution. The sodium hydrox-

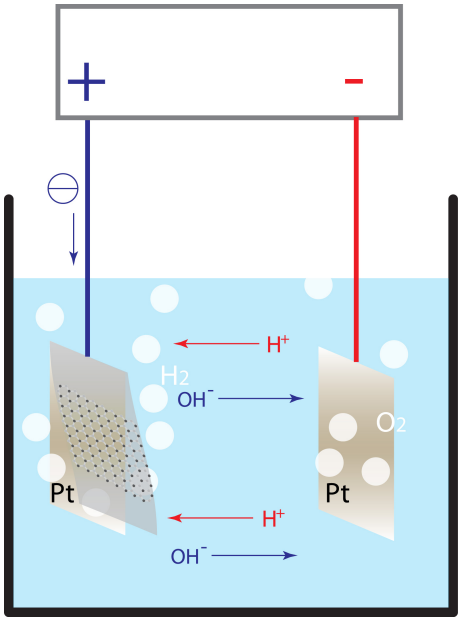


Figure 1.5: Schematic of the electrolysis system for graphene transferring.

ide increases the conductivity of electrons and when a 1 A current is applied, the following reactions happen at the cathode:

$$2\,\mathrm{H^+} + 2\,\mathrm{e^-} \longrightarrow \mathrm{H_2(g)}, \tag{1.15}$$

and at the anode:

$$4\,\mathrm{OH^-} \longrightarrow 2\,\mathrm{H_2O} + \mathrm{O_2(g)}. \tag{1.16}$$

Hydrogen gas is generated between the graphene layer and the platinum foil and the graphene detaches itself from the platinum. It takes about 15 seconds to "peel" the graphene/PMMA membrane from the platinum foil. The detached membrane is washed in de-ionized water and transfered to a substrate such as silicon dioxide or TEM sample holder. Then acetone is used to roughly remove PMMA. A thorough removal of PMMA requires hydrogen annealing. The general ambient-pressure recipe for PMMA removing is: 300 sccm of argon, 700 sccm of hydrogen,

ramping from room temperature(RT) to temperature between 300° C and 350° C in two hours, standing by that temperature for an hour and dropping to RT by shutting the furnace power down.

The electrolysis method is etchant-free and metallic-residue-free. The only residue on graphene, PMMA, could be almost fully removed by annealing. A small amount of PMMA residue is acceptable in TEM darkfield investigation and transport measurements. The only occasion I need to pay special attention to the residue is when I am trying to obtain high resolution TEM (HRTEM) images. When copper is used as the catalyst, however, I observed significant amount of copper residue on graphene after the wet-etching process.

## 1.5 Characterization of Graphene

The characterization of graphene as a single-layer atomic thick material is a challenge to experimentalists and has received much attention. Graphene probably has been characterized by all normal methods in surface physics such as optical microscopy[3, 21], atomic force microscopy(AFM), SEM[22], Raman microscopy[21], scanning tunneling microscopy(STM)[23] and TEM[24, 25, 26, 27, 28].

Optical microscopy is used to distinguish layer number of thin graphene samples[3, 29]. As the first-step for most characterization, this method has a low optical-level resolution ($\mu$m) and is prone to be confounded by the presence of residues on or under graphene. Raman spectroscopy is a widely-used and effective method to characterize layer number and stacking order of exfoliated few-layer graphene[8, 29],

but for graphene synthesized by chemical vapor deposition or epitaxial growth on SiC, it often does not show clear signatures of Bernal stacking[21, 30]. Similar to optical microscopy, Raman microscopy as a technique using laser detection is also limited in spatial resolution by optical wavelength, as in Appendix A.

AFM may reach quasi-atomic resolution, but absolute measurement of layer number is difficult on continuous graphene or samples with residues. STM with an atomic resolution has been used to investigate the roughness[23] of graphene samples and electron-hole puddles[31, 32] with the disadvantage of slow scanning and a crucial requirement of the sample cleanness. Generally speaking, it cannot be used to identify layer-number and stacking-order for continuous graphene as in AFM even though Morié patterns in an STM image can be used to identify stacking of bi-layer graphene[33].

Electron microscopy, which will be introduced in Section 1.6, can be used to image graphene structure on nanometer scales in the presence of PMMA residue. SEM as a convenient method was used to identify the layer number of graphene[22] though it lacks the ability to identify crystal orientation. As one of the most prominent methods, TEM is used broadly: high angle annular dark field scanning transmission electron microscopy (STEM) coupled with electron energy loss spectroscopy has been shown to distinguish graphene layer number[34]; real-space high-resolution TEM images have also been analyzed to distinguish between monolayer and multi-layer graphene[24]; electron diffraction has given information in graphene layer number and stacking order[28, 35]; dark-field TEM (DF-TEM) has been used to characterize the polycrystalline structure of graphite or single-layer

graphene[25, 26, 27, 35].

Table 1.1 summarize the pros and cons of these characterization methods. It is clear that TEM is the only method by which both layer-number and stacking-order of CVD graphene can be obtained.

Table 1.1: Pros and cons of characterization methods for graphene. Here symbol ☺ means that the method gives convincing and positive result about the information needed on the left column, ☹ means negative results and 😐 means that the method can provide certain information with significant uncertainties.

| | optical | AFM | SEM | Raman | STM | TEM |
|---|---|---|---|---|---|---|
| convenience | ☺ | ☹ | ☺ | ☺ | 😐 | 😐 |
| resolution | ☹ | ☺ | ☺ | ☹ | ☺ | ☺ |
| in situ | ☹ | 😐 | ☺ | 😐 | ☺ | ☹ |
| layer number | 😐 | ☺ | 😐 | ☺ | ☹ | ☺ |
| stacking order | ☹ | ☹ | ☹ | ☺ | 😐 | ☺ |
| CVD sample compatible | ☹ | ☹ | ☺ | ☹ | 😐 | ☺ |

## 1.6 Introduction to Transmission Electron Microscopy

As discussed in Section 1.5, TEM is one of the most prominent method to characterize the atomic-scale structure of graphene. We introduce TEM by starting with the electron microscopy[36, 37].

As a sample is exposed to electron beam, various physical phenomena take

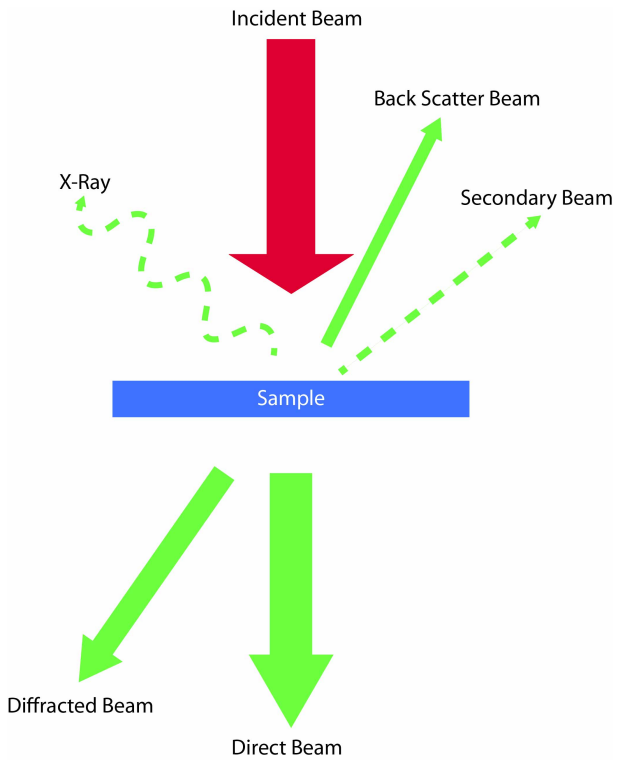


Figure 1.6: Signals generated in electron-material interaction. The strength of electron beams are shown roughly proportional to the width of the beam. Those generated in elastic processes are presented by solid lines while those in inelastic process are in dashed lines. Electron beams are straight lines while X-rays are wavy.

place, carrying information of the sample's crystallography, morphology, configuration, components, etc. For a thin sample, as shown in Figure 1.6, majority of the incident beam passes directly through the sample, forming a bright-field image. The thickness of the sample correlates with contrast in the image: thicker regions are always darker than thinner regions as might be expected. A small portion of electron beam scattered by the sample atoms can be used to form dark-field image or diffraction pattern, depending on whether the microscope lenses are set up in image mode or diffraction mode as explained in detail below. Thus there is a one-to-one corre-

spondence between dark-field image and diffraction pattern. The diffracted beam contains abundant information of the crystalline of the sample: grain boundary, phase, orientation, etc. Contrary to bright field images and perhaps to intuition, the contrast in the dark field images is inverse to the thickness: a thicker region is brighter than a thinner one. That is because a thicker region contributes more scattered electrons than a thinner region in constructive interference. The direct beam and the diffracted beam are the two main electron signals used in TEM.

A parallel beam source of electrons is used in TEM, whatever in image mode or diffraction mode. When the beam is concentrated into a nano-size spot on the sample, convergent beam electron diffraction (CBED) occurs. By scanning the spot over the sample, scanning transmission electron microscopy (STEM) image is obtained with abundant information on the roughness and morphology of the sample.

For thick samples, all electrons are scattered back and secondary electron microscopy (SEM) uses a detector placed right above the sample. Elastically back scattered electrons contain the information of crystal structure, as the electron signal used in electron backscattering diffraction (EBSD), with which we identify the crystal orientation of Pt foil in the thesis in Chapter 3. Inelastically scattered, or secondary, electrons have low energy and they are mainly used to provide nano-scale resolution images.

X-rays are also generated in inelastic collision of electrons with atoms, when an electron is excited and transits back to the ground state. Thus the frequency or energy of the X-ray depends on the atom excited and can be used to identify the

components of the material investigated. Two elements, hydrogen and lithium, are not detectable with this method because of the low energy of the signal generated (or "too light" in the language of electron microscopy). Both TEM and SEM can take advantage of this signal and such technology is called energy-dispersive X-ray spectroscopy (EDX).

Now we discuss the imaging principles of TEM in detail. The simplified optical path diagram is shown in Figure 1.7. Passing through condenser lenses, objective lenses, and projective lenses, electrons converge into bright spots indicating the crystal structure of the sample, the so called diffraction mode, or form image of the sample, the so called image mode. In the diffraction mode, the brightest center spot (1) is formed by electron passing right through the sample, the direct beam; the weaker spots (2) bearing certain symmetry arise from electron diffraction by crystal facets. In both modes, the optical path is exactly the same above a plane under the objective lens, the so-called focal plane. By placing an objective aperture in the focal plane to select either spot (1) or (2) in Figure 1.7, the electron beam with certain diffraction angle is selected. Therefore there is a one-to-one correspondence between a diffraction spot and a dark field image. Switching from the diffraction mode to the image mode, either a bright field image or dark field image corresponding to the selected spot is obtained. The bright field image has little contrast, especially for thin samples such as graphene, and the thicker region of the sample is shown to be darker. The dark field image, on the contrary, provides abundant information of the crystal structure and shows the opposite relationship between thickness and intensity: the thicker part of the sample is brighter in the image.

The technique discussed above is especially effective with thin materials such as graphene. It can be used to identify the orientation of polycrystal graphene[27]. In the six-fold symmetry diffraction pattern of graphene, there are $6n$ diffraction spots for each order, which is determined by the order of primitive vector in reciprocal lattice. Here $n$ indicates the number of regions with different crystal orientations. The relative angle of the orientation of a crystallite is demonstrated directly by the rotating angle of one set of diffraction spots with respect to another. In the image mode, a part that is bright in one dark field image and totally black in others indicates that it shares a different orientation with the other parts.

An important part of this thesis is the powerful technique developed using selected area electron diffraction (SAED) and DF imaging to quantitatively determine the layer number and stacking sequence of graphene[35], which will be discussed in Chapter 2.

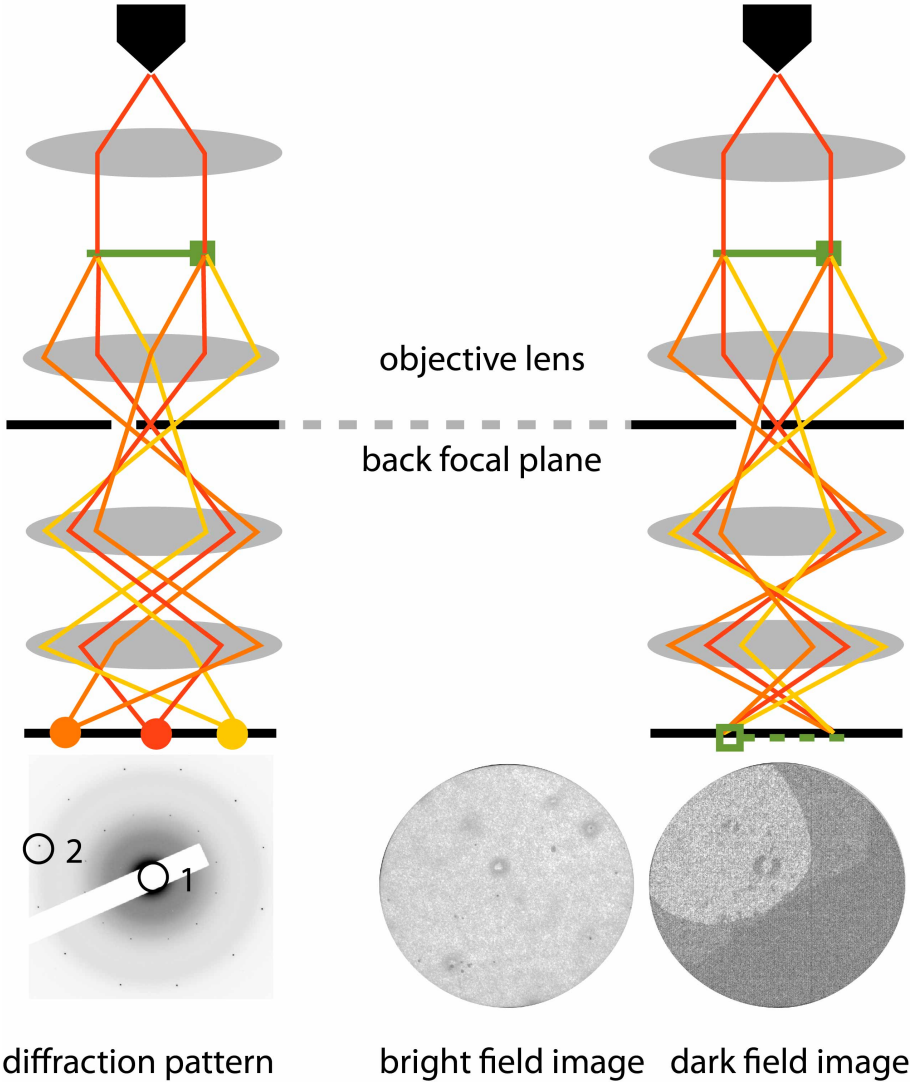


Figure 1.7: Optical path diagram of the diffraction mode (left) and the image mode (right) of TEM. The image mode can generate either a bright field image or a dark field image by selecting, with an aperture placed in the diffraction pattern, the direct beam (1) or the diffracted beam (2) respectively.

# Chapter 2

# LAYER NUMBER AND STACKING ORDER IDENTIFICATION OF GRAPHENE BY ELECTRON DIFFRACTION

In this chapter I introduce the dark-field electron microscopy technique based on SAED patterns and DF images of TEM. This method is applied to identify the layer number and stacking order of Pt-grown graphene up to seven(7) layers[34, 35] and characterize grain boundaries of graphene and pyramid-like mulitlayer structure. The results of this study have been published in Ref.[35]. Armed with this technique, I discovered nanocrystalline graphene impurities under the Pt-grown continuos crystalline monolayer graphene sample and understood the crystallity and morphology of such impurities shown in Chapter 3. It is the characterization by electron microscopy that provides us with clues to understand the abnormal magneto-transport behavior of our graphene samples, as discussed in Chapter 4.

Using kinematical theory, I calculated the first- and second-order diffraction intensities of multi-layer graphene of arbitrary stacking (arbitrary number of layers on A, B, or C sites of the hexagonal lattice). For simple samples (layer number $n \leq 3$), the intensity ratios of first- and second-order SAED spots measured match with theory. Real-space DF images are used to produce maps of layer number contrast with few-nanometer spatial resolution. For complex heterogeneous multilayer graphene samples with layer number n $\leq$ 7, we use contrast in DF images

to unambiguously distinguish the layer-number and stacking-order. We find that multilayer graphene exhibits Bernal (ABAB) or rhombohedral (ABCABC) stacking correlations across multiple layers.

## 2.1 Electron Diffraction by Graphene

Electrons as source particles provide more detailed information than x-rays, let alone optical microscopy. Both electrons and x-rays are diffracted by crystal lattices but electrons have a wavelength (3.7 pm at 100 keV) 3.7% of that of x-rays (100 pm). Thus microscopy techniques based on electron scattering can give much higher resolution. The radius of the Ewald sphere formed by an electron($K_0 = 170$ Å$^{-1}$) is about 30 times larger than that by an x-ray(6.3 Å$^{-1}$), meaning more deflection. The diffraction angle of diffracted electrons ranges from 0° to 2° in contrast to 0° to 180° of x-ray. Thus the diffracted electron beams are close to the direct(undiffracted) beam, making it possible to select a diffracted beam from diffraction pattern with an aperture. What is more, the interaction of electrons with the investigated matter is $10^6$ to $10^7$ times greater than that of x-rays, so that the diffracted electron beam has a high intensity and the exposure time is short (typically several seconds) and more microscopic information is extracted from the interaction, elastic or inelastic, as in Section 1.6.

Our calculation of electron diffraction by graphene is based on the kinematic approximation that the interaction of an electron with an atom is so transient that the carbon atom can be seen as a rigid body[36]. The electronic structure of a

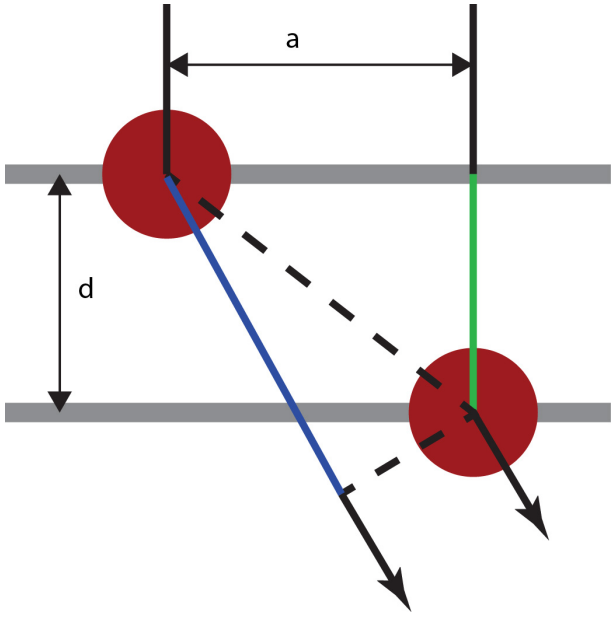


Figure 2.1: Electron diffracted by carbon atoms located on different layers. The parameters are given in Chapter 1. The path colored in blue and green corresponds to parts with the same color in Equation 2.2.

single carbon and crystal structure of multilayer graphene, as shown in Figure 1.2 in Chapter 1, contains the full information needed to calculate the diffraction pattern. The intensity can be written as

$$I = I_0 \times \xi, \tag{2.1}$$

where the atomic scattering intensity $I_0$ arises from the electron structure of a carbon atom and the modulation term $\xi$ contains crystallographic information about the graphene lattice.

As given in Chapter 1, the length of the primitive vector in the reciprocal lattice is $b = 4\pi/a\sqrt{3} = 2.95\text{Å}^{-1}$. Thus we have lengths of the first order and second order primitive vectors in the reciprocal lattice: $K_1 = b = 2.95\text{Å}^{-1}$ and

$K_2 = 5.11\text{Å}^{-1}$.

A schematic of electron diffraction by bilayer graphene is shown in Figure 2.1. The path difference is

$$\begin{aligned}\Delta &= \frac{d}{\cos\theta} + (a - d\tan\theta)\sin\theta - d \\ &\approx a\theta \end{aligned} \tag{2.2}$$

where $\theta = K_i/K_0$ is approximately 0.017 for $K_i = K_1$ or 0.03 for $K_i = K_2$. Here $K_0$ is the radius of the Ewald sphere.

The meaning of Equation 2.2 is that for electron scattering by few-layer graphene, atoms located on different layers can be treated as if they were on the same layer: a three-dimensional crystal is "squeezed" into a two-dimensional crystal. With this view point, the calculation of electron diffraction is greatly simplified.

The modulation term $\xi(\mathbf{K})$ in Equation 2.1 is the square modulus of the structure factor $f(\mathbf{K})$:

$$\begin{aligned}\xi(\mathbf{K}) &= |f(\mathbf{K})|^2 \\ &= |\sum_i e^{i\mathbf{K}\cdot\mathbf{r}_i}|^2. \end{aligned} \tag{2.3}$$

We define the stacking mode to represent the stacking order of layers of graphene. An ABABC stacking graphene, for example, has stacking mode (2,2,1). The structure factor can be analytically calculated by noticing that a stacking mode A contributes a term $1 + e^{i\frac{4}{3}\pi(n_1+n_2)}$, B a term $e^{i\frac{2}{3}\pi(n_1+n_2)} + e^{i\frac{4}{3}\pi(n_1+n_2)}$ and C a term

$1 + e^{i\frac{2}{3}\pi(n_1+n_2)}$. The modulation term $\xi$ for an arbitrary stacking is

$$\xi = \begin{cases} (a+b+c)^2 = 4n^2 & \text{if } n_1 + n_2 = 3k,\ k \in \mathbb{Z} \\ \frac{1}{2}\left[(a-b)^2 + (b-c)^2 + (c-a)^2\right] & \text{if } n_1 + n_2 \neq 3k,\ k \in \mathbb{Z}, \end{cases} \tag{2.4}$$

where $a$, $b$ and $c$ are one of 1, $e^{i\frac{2}{3}\pi(n_1+n_2)}$ and $e^{i\frac{4}{3}\pi(n_1+n_2)}$ and $n_1$ and $n_2$ are integers which equal to $\mathbf{K}\cdot\mathbf{r}_i/2\pi$. The valid values of $\mathbf{K}$ are primitive vectors in the reciprocal lattice which starts from first order $\mathbf{K}_1$ to infinity.

Provided with stacking order, we can have the stacking modes and obtain $\xi$ for first and second order diffraction by Equation 2.4, as shown in Table 2.1 and Figure 2.2. It can be seen that $\xi_2 = \xi(\mathbf{K}_2)$ varies quadratically with layer number. Thus the intensity of the second order diffraction alone is sufficient to discriminate between different layer numbers. In the case of $\xi_1 = \xi(\mathbf{K}_1)$, and hence first order diffraction intensity, the magnitude depends on layer number and structure. There are degeneracies, however, such as for the monolayer and bilayer. So the ratio of first- to second-order intensities, which is written as

$$\frac{I_1}{I_2} = \frac{I_{01}}{I_{02}}\frac{\xi_1}{\xi_2}, \tag{2.5}$$

is used as an indicator of stacking order; $I_1/I_2$ is evaluated for 100 keV incident electrons and listed in the last column of Table 2.1 and Figure 2.3. It should be noted that for 100 keV accelerating voltage, the intensity ratio of atomic scattering by electrons is $I_{01}/I_{02} = 4.49$[38]. Single layer graphene (and all AA stacked graphene) has the highest $I_1/I_2$ ratio of 1.12. Bernal stacked graphene tends to converge to a ratio 0.3, and rhombohedral graphene to a ratio 0 (i.e. the first-order spot is missing). Thus for layer number $n \leq 3$, the ratio clearly identifies all possible layer

numbers and structure models. For large layer number, the ratio gives some contrast between regions of differing layer number (especially differing by one layer) and is particularly sensitive to the presence of stacking faults.

Table 2.1: Diffraction pattern parameters for various structure models. The structure model means stacking mode. For example, structure model 1,2,1 means a layer of graphene in A stacking position, two layers in B position and one in C position.

| Layer Number | Structure Model | $\xi_1$ | $\xi_2$ | $I_1/I_2$ |
|---|---|---|---|---|
| 1 | 1 | 2 | 8 | 1.12 |
| 2 | 1,1 | 2 | 32 | 0.28 |
| 3 | 1,2 | 6 | 72 | 0.37 |
| | 1,1,1 | 0 | | 0 |
| 4 | 1,3 | 14 | 128 | 0.49 |
| | 2,2 | 8 | | 0.28 |
| | 1,1,1 | 2 | | 0.07 |
| 5 | 1,4 | 26 | 200 | 0.58 |
| | 2,3 | 14 | | 0.4 |
| | 1,3,1 | 8 | | 0.31 |
| | 2,2,1 | 2 | | 0.04 |
| 6 | 1,5 | 42 | 288 | 0.65 |
| | 2,4 | 24 | | 0.37 |
| | 3,3 | 18 | | 0.28 |
| | 1,1,4 | 18 | | 0.28 |
| | 2,3,1 | 6 | | 0.09 |
| | 2,2,2 | 0 | | 0 |

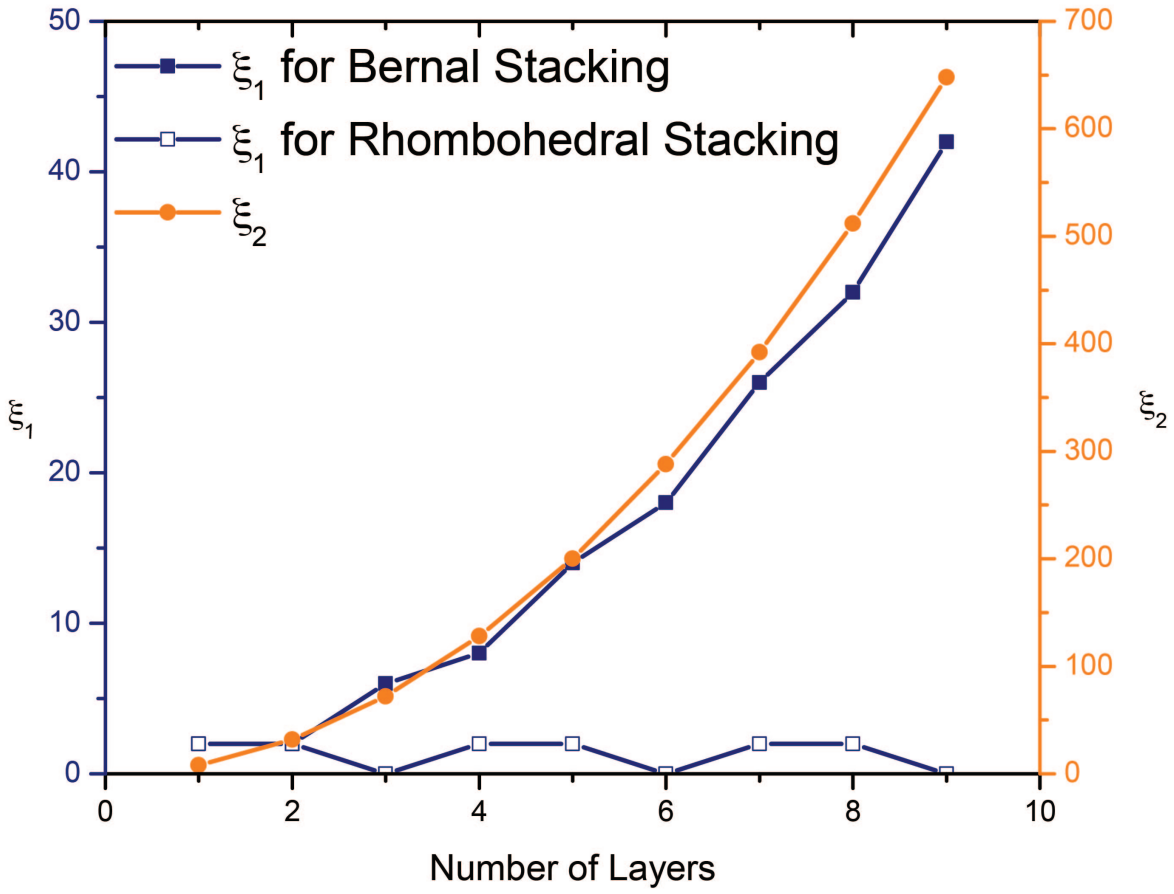


Figure 2.2: Kinematical calculation of the modulation factor $\xi$ of electron diffraction of graphene. The curves show $\xi_1$ for Bernal and rhombohdral stacking and $\xi_2$ obtained from Table 2.1. Note the layer-number-identification ability of $\xi_2$ despite the stacking order.

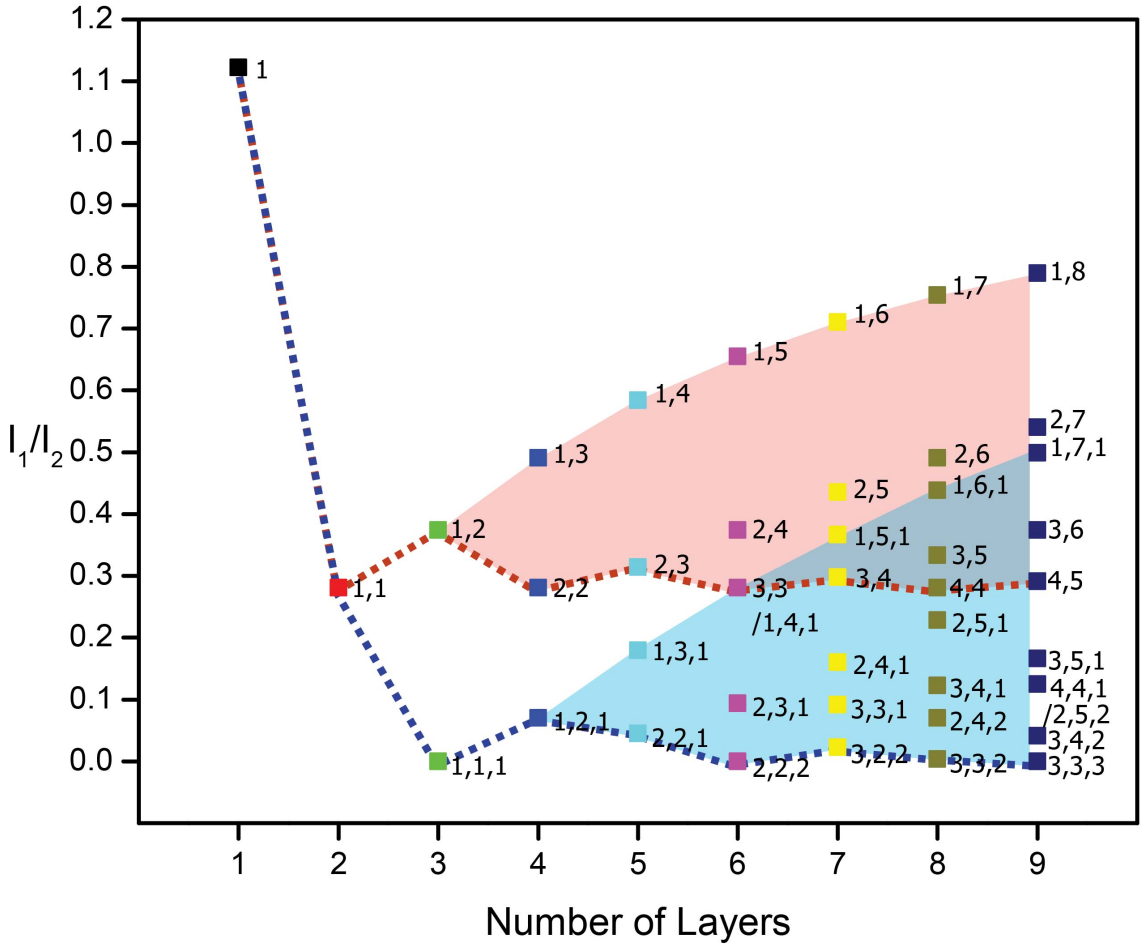


Figure 2.3: Kinematical calculation of intensity ratios for electron diffraction of graphene extracted from Table 2.1. Squares are electron diffraction intensity ratios for first- and second-order diffraction spots as a function of layer number. The structural model is denoted using the notation described in the text. The dashed red line connects structure models representing Bernal stacking, and the dashed blue line connects structure models representing rhombohedral stacking. The shaded pink and blue regions enclose structure models containing two elements (AB) and three elements (ABC) respectively. The numbers on the right side of each colored square are structure models as in Table 2.1. Note that there are degeneracies existing for certain models.

## 2.2 Characterization by Dark Field Image

The samples used in this section were grown on platinum at 1040° C in the gas mixture of hydrogen (700 sccm) and methane (5 sccm) and transfered to a silicon dioxide wafer or silicon TEM sample holders with a 1.0 mm x 1.0 mm window covered by 50 nm thick silicon nitride membrane. While the samples are dominantly monolayer graphene, I also find heterogeneous multi-layer graphene structure which are characterized in this section. Figures 2.4(a) and (b) show bright-field images of stepped-pyramid structures of small graphene crystallites. The second-order dark field images (Figures 2.4(c) and (d)) clearly distinguish the presence of many discrete layer number regions with sharp boundaries. Interestingly, the first-order dark-field images show regions of different contrast within each terrace of constant second-order contrast, which we interpret as regional areas of different stacking order as verified below. Note that in one sample (Figures 2.4(a), (c), (e)) there is an additional single graphene layer covering the upper portion of the image which is slightly rotated with respect to all the other layers, producing a Moiré pattern (this was verified by noticing that the Moiré pattern orientation rotated according to the diffraction spot used to produce the image).

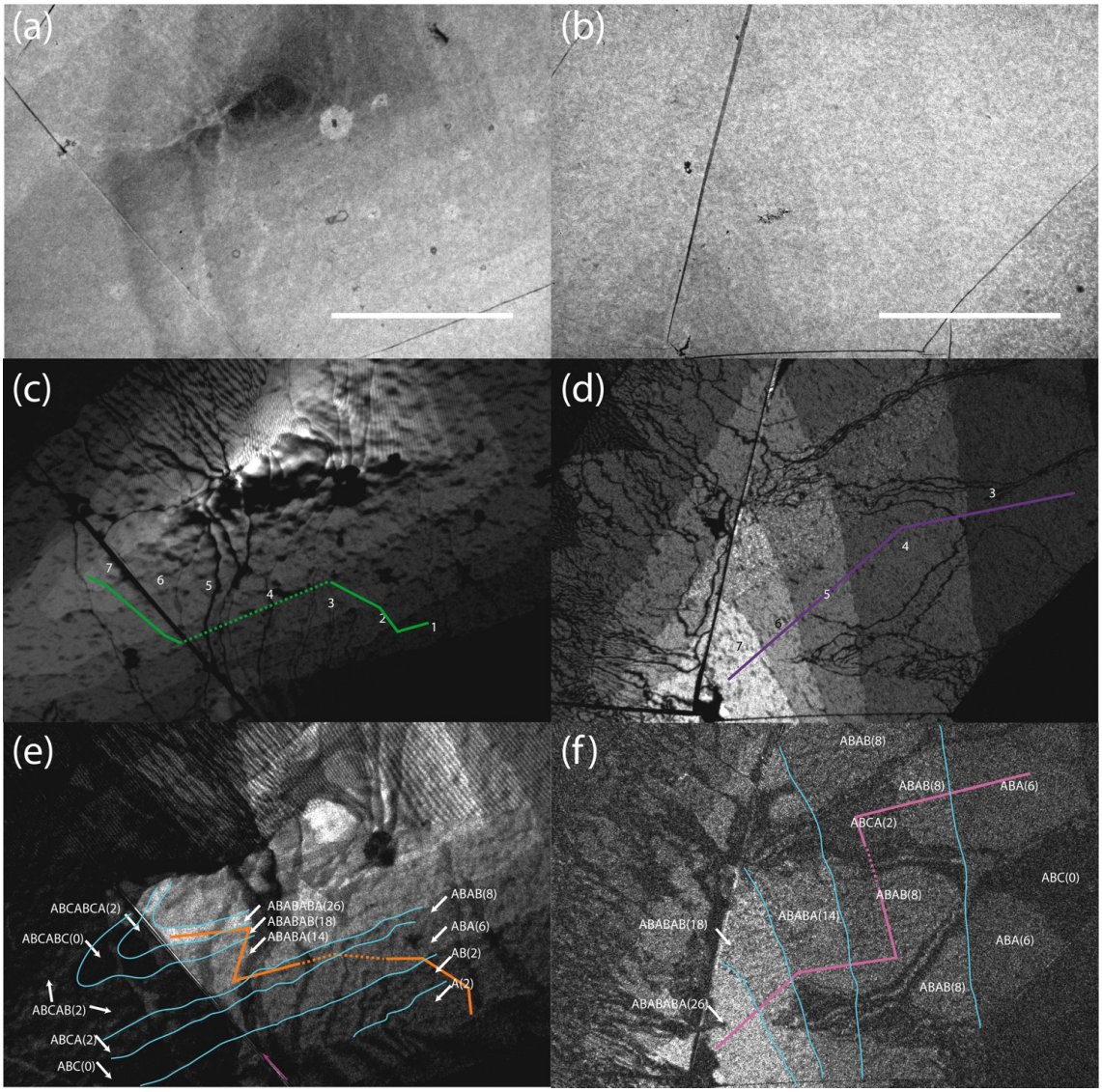


Figure 2.4: Bright-field images (a) and (b) of two samples can barely distinguish layers. The scale bars are 500 nm. Second order DF images (c) and (d) and first order DF images (e) and (f) corresponds to (a) and (b) in the same column with the same scale. Cyan contours in (e) and (f) are obtained from (c) and (d), which are sufficient to give layer-number, as labeled. Stacking order are labeled in (e) and (f) with values of $\xi_1$ in parenthesis. The boundary of Bernal and rhombohedral stacking in (e) is indicated by the purple arrow. The segmented lines in (c-f) correspond to intensity profiles shown in Figure 2.5.

I assigned stacking orders to the various regions in Figure 2.4 as follows. I notice that for a given second-order intensity there are at most two different first-order intensities. Therefore I assume that there are only two types of stackings: Bernal (AB) and rhombohedral (ABC). I assign the higher-intensity first-order areas as Bernal stacked, and lower-intensity areas as rhombohedrally stacked. The stacking assignments are denoted in Figures 2.4(e) and (f). In Figure 2.4(e), there is a sharp boundary (purple arrow) between rhombohedrally-stacked graphene on the lower left, and Bernal stacking on the upper right. The first-order intensity grows monotonically with layer number for the Bernal-stacked region, but is low and non-monotonic in layer number for rhombohedrally-stacked graphene, in qualitative agreement with Figure 2.2(a). Similar but less sharply-defined regions of rhombohedral stacking are observed in Figure 2.4(f).

I now analyze the first- and second-order diffraction contrast quantitatively. Figures 2.5(a), (b), (c), (d) show line profiles along the colored lines in Figures 2.4(c), (e), (d), (f) respectively. I take averages over the regions denoted by horizontal lines (the vertical position of the line shows the average) which are identifiable on the dark-field images as areas of uniform contrast. Figures 2.5(e)-(h) show the average contrast values for each region in Figures 2.5(a)-(d) plotted versus the expected contrast (see Figure 2.2(a)). There is an offset in the experimental values mainly due to a diffuse background in the dark-field images due to the presence of the silicon nitride membrane. For this reason I used the diffraction contrast directly instead of the quantity $I_1/I_2$. The linear relationship in Figures 2.5(e)-(h) indicates agreement between experiment and theory. The experiment shows the fine details

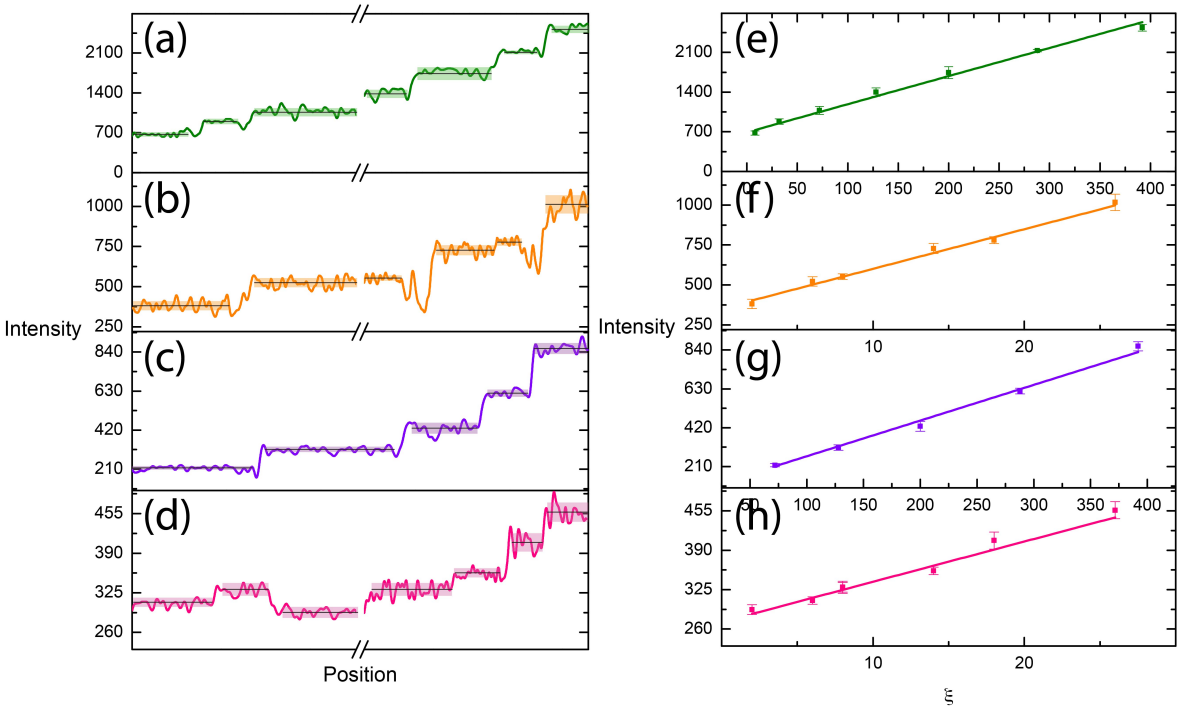


Figure 2.5: Intensity profiles (a-d) correspond to the same-color segmented lines in Figures 2.4(c)-(e). The break points corresponds to the dashed line segments. Horizontal lines and shaded regions denote the mean value and standard deviation of the intensity averaged over each segment. Experimentally determined mean intensities (e)-(h) as a function of the theoretically calculated values from Table I for the structure assignments indicated in Figures 2.4(c)-(e). A linear relationship indicates agreement between experiment and theory.

of the theory: The second-order intensity varies quadratically with layer number (Figures 2.5(e),(g)). For Bernal and rhombohedral stacking within the same layer number (Figure 2.5(h); ABCA vs. ABAB) the experiment shows the expected relative intensities. For Bernal stacking the first-order diffraction intensity (Figure 2.5(f)) rises with layer number monotonically but non-uniformly [for example,

ABA (6) and ABAB (8), and ABABA (14) and ABABAB (18) are relatively closely spaced in intensity]. We note that because of the background, absolute layer thickness determinations from measurement of only one or a few structures would be difficult with our technique, but the situation could be significantly improved by suspending the graphene.

I now discuss the observation of different stacking sequences in the same sample. The coexistence of rhombohedral and Bernal stacking had been previously observed in Raman microscopy on trilayer graphene. Here the TEM technique, with high spatial resolution, has allowed me to make two new observations: First, I observe that stacking correlations (rhombohedral vs. Bernal) persist over several layers (up to seven layers in Figure 2.4(e)). This is quite surprising given the weak interlayer interactions in graphene. Second, I observe that most boundaries between rhombohedral and Bernal stacked regions appear to be associated with out-of-plane deformation or wrinkling of graphene (seen as a dark contrast in the second-order dark-field images Figures 2.4(c) and (d)). This suggests mechanical stress as either a cause or a result of the stacking fault boundary. The very straight boundary between rhombohedral and Bernal stacking seen in Figure 2.4(e) appears somewhat unusual compared to the meandering lines that we presume are wrinkles; I am unsure of the origin of this feature.

## 2.3 Characterization by Diffraction Pattern

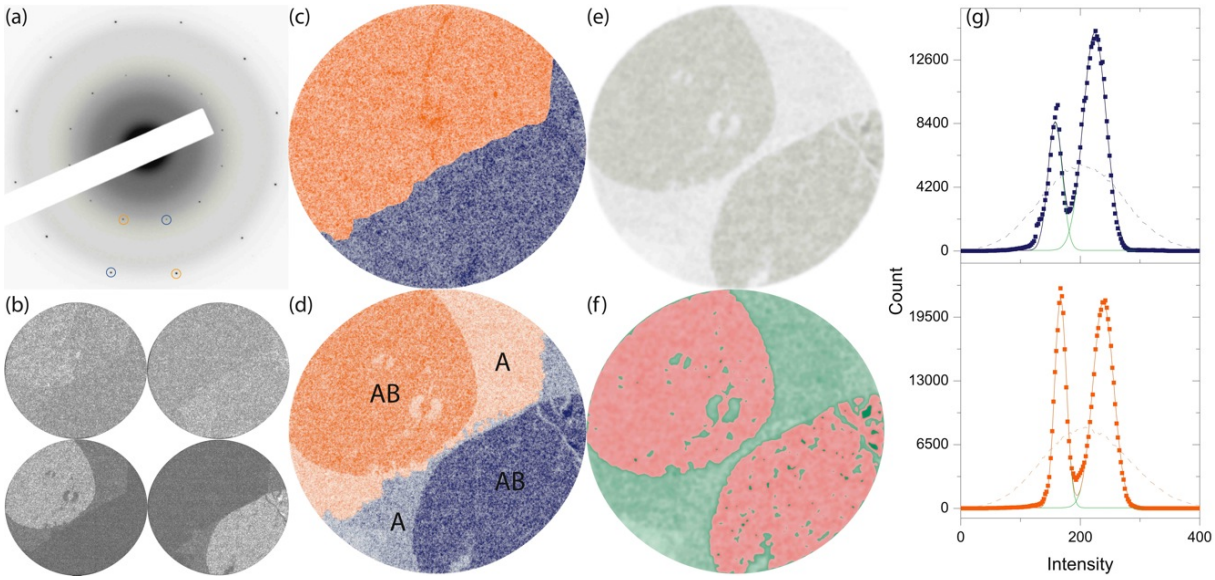


Figure 2.6: SAED pattern (a) and corresponding raw DF images (b) of a sample hydrogen etched for 30 minutes. Combined dark field images (c, d) for first-order (c) and second-order (d) diffraction spots. Color corresponds to crystallographic orientation as indicated in (a). Index in (d) are structure models. (e) Grey scale image of ratio of first-order to second-order diffraction intensity. (f) Same image as (e), colored to indicate areas of single-layer graphene (green) and Bernal stacked bilayer graphene (red). (g) Histograms of the intensities of the DF image (d) for blue (upper panel) and orange (lower panel) crystallographic orientations. The dashed lines indicate histograms of the raw image, and the solid points indicate histograms after Gaussian filtering the images at 4.8 nm. The solid lines are fitted to two Gaussians, with individual Gaussian components indicated by green lines. The diameters of all DF images are 1$\mu$m.

I now give another quantitative example of our imaging technique. The sample in this case is graphene deposited and annealed on copper and transfered as described

in Section 1.3 in Chapter 1. From selected area electron diffraction (SAED) studies I determine that the multi-layer graphene crystallites grown by this method in most cases (95%) show crystallographic alignment among all the layers. Rare overlap of graphene layers with different orientations is identified by Moiré patterns in DF images.

Figure 2.6(a) shows a typical SAED pattern which indicates that two different crystallographic orientations (two grains) are present. Four raw DF images in Figure 2.6(b) correspond to the first and second order diffraction spots for the two crystallographic orientations (orange or blue circles in (a)). The data of raw DF images are converted to grey scale and area of graphene are isolated by applying a threshold on the grey scale mapping. They are then colored, orange or blue respectively corresponding to the two crystallographic orientations, with intensity corresponding to the greyscale value, and merged and inverted to generate Figure 2.6(c) (for DF images corresponding to first order spots) and Figure 2.6(d) (second order spots). Based on the one-to-one correspondence between SAED patterns and DF images, regions with different colors (orange, blue) represent graphene with different orientations. The first order DF image ( Figure 2.6(c)) shows no layer number contrast, as expected from $I_1$ in Table 2.1, while the second order DF image shown ( Figure 2.6(d)) demonstrates clear contrast within each crystallographic region. As Table 2.1 indicates, the second order SAED pattern, and thus its corresponding DF map, is sufficient to distinguish layer number. Hence dark and light regions in (d) correspond to thicker layer and thinner regions respectively.

In order to generate a map of layer number contrast alone, the raw second

order DF images in (b) are added and then Gaussian filtered with a 6 pixel variance (4.8 nm), resulting in image (e). A histogram of the intensities in (e) shows two well-resolved peaks indicating two contrast level are well-resolved at 4.8 nm resolution. (The histogram of the raw image shows only one peak.) Setting the threshold between the two peaks allows the image to be colored corresponding to the areas of different layer number ( Figure 2.6(f)). Moreover, the histogram also measures the areas of graphene with different layer numbers but the same orientation, which are proportional to the areas enclosed by each peak, and the total area of graphene with each orientation, which is proportional to the area enclosed by the whole fitting curve.

Table 2.2: Determination of the structure model of the graphene samples shown in Figure 2.6. The experimental quantities $I_1/I_2$ and $I_k^{(m)}/I_k^{(n)}$ and the theoretical results for the structure model are shown. Sign "&" in the Structure Model column represents the coexistence of two or more structure models with the same crystal orientation. Percentages in Structure Model column represent the fraction of area with that structure determined experimentally from histograms (Figure 2.6(g)).

| Region | $I_1/I_2$ | | $I_1^{(o)}/I_1^{(b)}$ | | $I_2^{(o)}/I_2^{(b)}$ | | Structure Model |
|---|---|---|---|---|---|---|---|
| | exp | theo | exp | theo | exp | theo | |
| orange | 0.39 | 0.38 | 1.54 | 1.51 | 1.34 | 1.37 | 1(36%)&1,1(64%) |
| blue | 0.34 | 0.35 | | | | | 1(27%)&1,1(73%) |

I now determine the layer number and structure model for the different regions

of the sample in Figure 2.6. The background of the SAED pattern is eliminated by a rolling-ball algorithm with ball radius 50 pixels, and intensities of SAED spots are obtained by integration over Gaussian peaks and then spots of the same order are averaged and the ratio $I_1/I_2$ is indicated in Table 2.2. A parameter $\beta^{(i)}$ that indicates the area portion of graphene with layer number index $i$ is evaluated from the area of peaks obtained from histograms (Figure 2.6(g)). For orientation-identical graphene with two different layer numbers, we have

$$\frac{I_1}{I_2} = \frac{\beta^{(i)} I_1^{(i)}/I_1^{(j)} + 1 - \beta^{(i)}}{\beta^{(i)} I_2^{(i)}/I_2^{(j)} + 1 - \beta^{(i)}} \times \frac{I_1^{(j)}}{I_2^{(j)}}. \tag{2.6}$$

The theoretical values of $I_1/I_2$ in Table 2.2 match the experimental data very well.

The quantity $I_1/I_2$ may not be accurate enough to identify layer numbers of complicated layer-mixed and/or many-layer graphene because (i) there is always more than one possible combination of structure model having values close to $I_1/I_2$ and (ii) the distribution of $I_1/I_2$ becomes denser as layer number increases, as shown in Figure 2.2. However, if there are multiple grains of different orientations, additional information is possible by comparing $I_k^{(m)}/I_k^{(n)}$, the ratios of intensity from SAED spots of grains $m$ and $n$ with the same order $k$. The additional ratios are shown in Table 2.2 for the sample shown in Figure 2.6; again, the theory matches with the experiment well.

Second-order DF images are also used to investigate my hydrogen-etched samples on a larger scale and I find thin graphene layers at the edges of crystallites, implying that etching always takes place at the boundaries between graphene single crystals, as in Figure 2.6. This technique also provides us with clues for under-

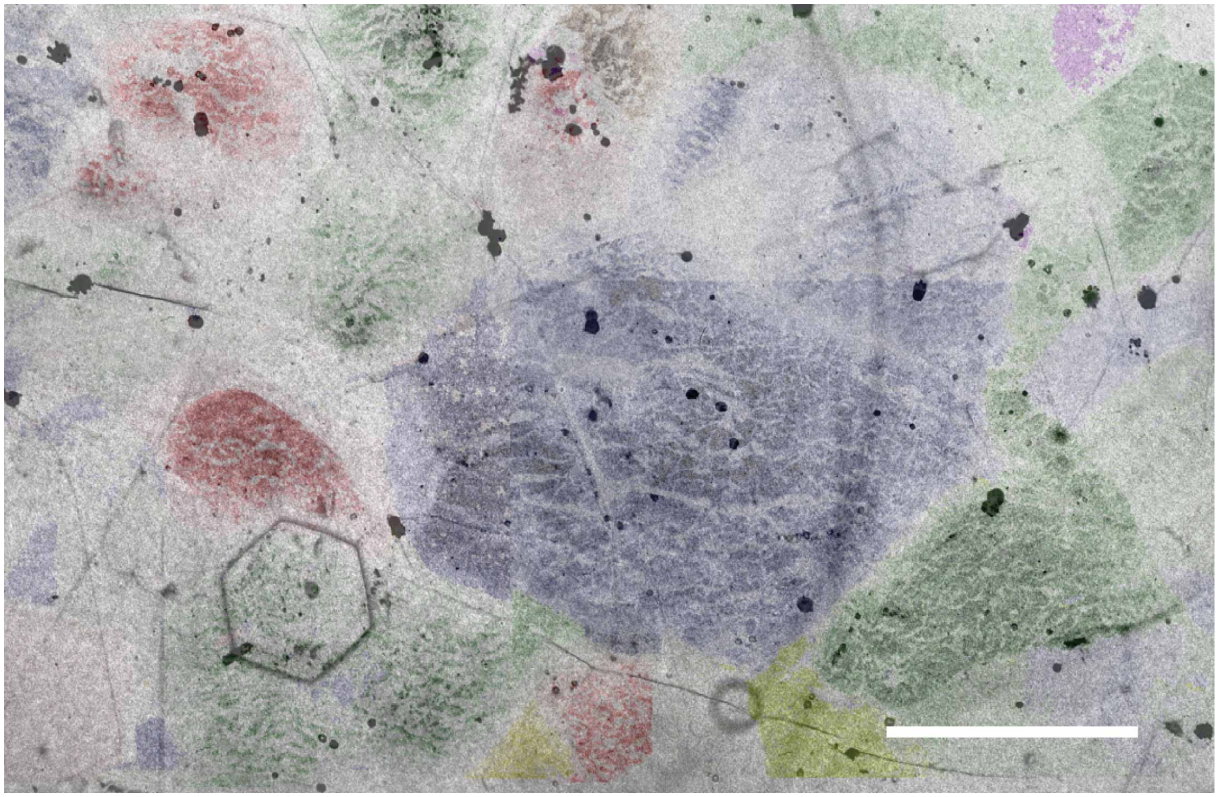

Figure 2.7: Second-order mapping of a typical graphene sample grown on copper. The scale bar is 1 $\mu$m. Graphene single crystals with the same orientation shares the same color in the image.

standing the growing processes of graphene. As shown in Figure 2.7, I observed long-range correlations of the graphene orientation indicating an effect of substrate lattice orientation growth of graphene on copper[39].

As another verification, I measured $I_1/I_2$ for single layer graphene flakes grown on copper as shown in Figure 2.8. The measured value turns out to be 1.03, within 10% uncertainty with respect to the theoretical value 1.1.

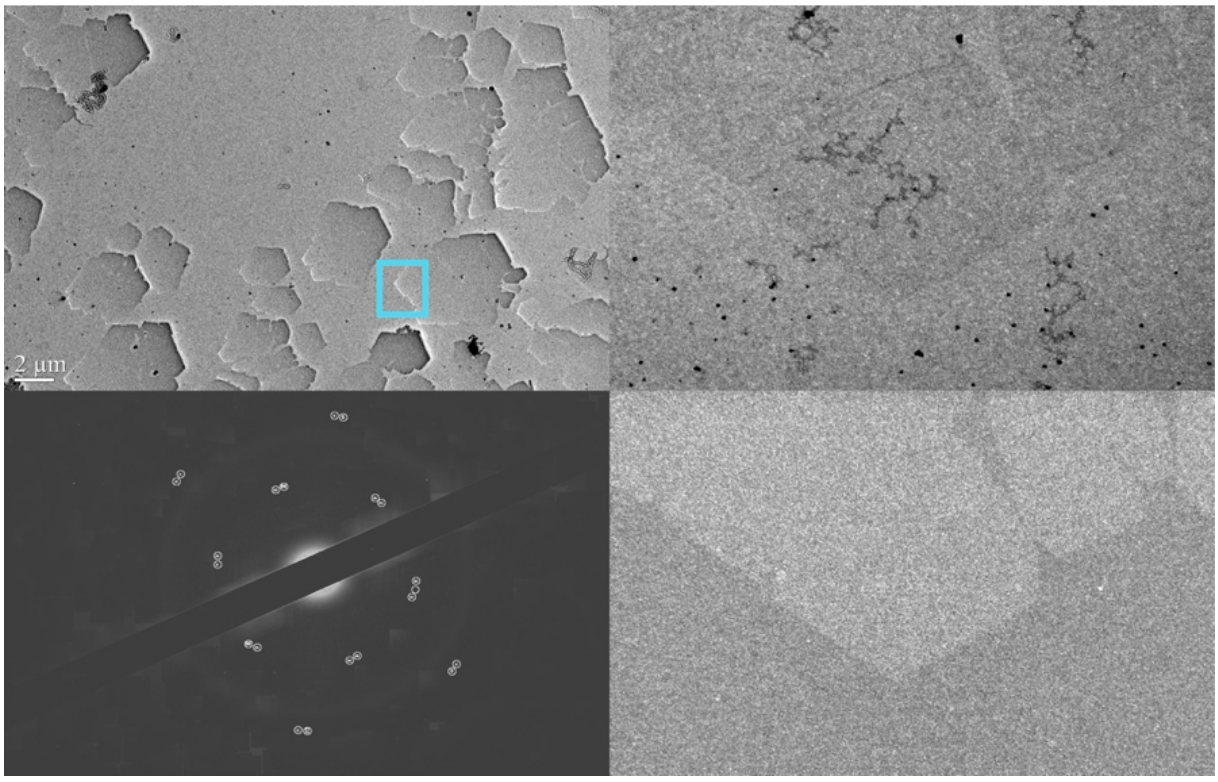


Figure 2.8: Top-left: TEM image of graphene single layer flakes grown on copper. Top-right and bottom-right: corresponding rotated bright field image and dark field image respectively with large magnification in the region enclosed by the blue rectangular in the top-left image. Bottom-left: background-substrated DP in the blue rectangular region. Each first or second order diffraction spots is marked and averaged with circles as indicated.

## 2.4 Disorder and Thermal Fluctuations

It is also worthwhile to address the robustness of our TEM technique to disorder or thermal fluctuations. The high Debye temperature of graphene indicates that corrections to $I_1/I_2$ due to the thermal Debye-Waller factor are on order 1% at room temperature[40]. Static disorder due to e.g. vacancies or adatoms[41] which

shift the atomic positions can lead to a static Debye-Waller factor[42]. However, point defects are easily detectable through the presence of a Raman D band. The Raman D to G intensity ratio is at most 0.3 in our samples (and often much lower), indicating a point defect concentration at most 100 ppm[43], which would lead to corrections to $I_1/I_2$ on order 100 ppm or less. Static disorder is therefore unlikely to significantly modify the analysis of our samples, or any technologically-relevant graphene samples with modest disorder.

# Chapter 3

# INTRINSIC CARBON IMPURITIES DECORATING CONTINUOUS MONOLAYER GRAPHENE

In the last chapter, the technique of characterization of graphene by dark-field TEM was brought out. In this chapter I discuss the use of this powerful technique combined with other methods such as optical microscopy, SEM, EBSD, TEM, HRTEM, AFM, Raman spectroscopy, and electrical transport measurements, to identify novel carbon impurity structures that have not been previously observed in Pt-synthesized graphene. These impurities consist of nanocrystalline $sp^2$ carbon, and can cause considerable confusion in characterizing the layer number and defect concentration of Pt-synthesized graphene by conventional methods.

## 3.1 Sample Preparation and Initial Characterization

The graphene samples were grown, as in Section 1.3 of Chapter 1, at 1000° C on a 0.2 mm thick platinum foil under a flowing ambient gas mixture of 700 sccm hydrogen and 5 sccm methane[5]. Figure 3.1(a) shows an SEM micrograph of the sample on Pt foil, and Figure 3.1(b) shows an optical micrograph of the sample after transfer to $SiO_2$/Si. As will be shown below, monolayer graphene covers the whole surface, but optical and SEM micrographs show few-micron-sized islands of increased contrast. Characterization of graphene on the Pt substrate via energy

dispersive X-ray spectroscopy (EDX) shows no significant peaks except carbon and Pt as in Figure 3.2. The size, morphology and configuration of the islands, as shown in Figure 3.1(a), depend on the crystalline orientations of the Pt substrate which are distinguished by contrast in SEM images due to the tunneling effect of secondary electrons. Such correlations will be investigated further via EBSD below in Section 3.2.

Typically graphene is transferred onto silicon dioxide substrates facing the same direction as it is on Pt, i.e. the side originally touching the metal surface touches the silicon dioxide surface after transfer. Imaging the topography of graphene transferred in this normal way requires removal of the transfer support, typically poly(methyl methacrylate) ( PMMA), in which case PMMA residue may contaminate the image. To investigate the topography of graphene grown on Pt without exposing the surface to be probed to PMMA, we use an up-side-down transfer method: we transfer the graphene/PMMA stack to $SiO_2$/Si with the graphene on top, and do not remove the PMMA.

Figure 3.1(c) shows an AFM image of graphene/PMMA transferred by the up-side-down method. The surface being imaged has no contact with PMMA. Islands similar in morphology to those seen in Figure 3.1(a) and (b) can be identified in the AFM image with height of about 0.35 nm to more than 1 nm. We also observed two types of wrinkles in graphene transferred by this method: raised wrinkles which were valleys in graphene on the Pt growth substrate and may represent the Pt metal grain boundaries, and indented wrinkles which were raised when graphene was on Pt, and likely arose from the differential thermal expansion between graphene and

Pt[4]. Such narrow wrinkles are not the consequence of the transfer process as graphene adheres tightly to the 300nm thick PMMA and only wrinkles close to that scale can result from transfer.

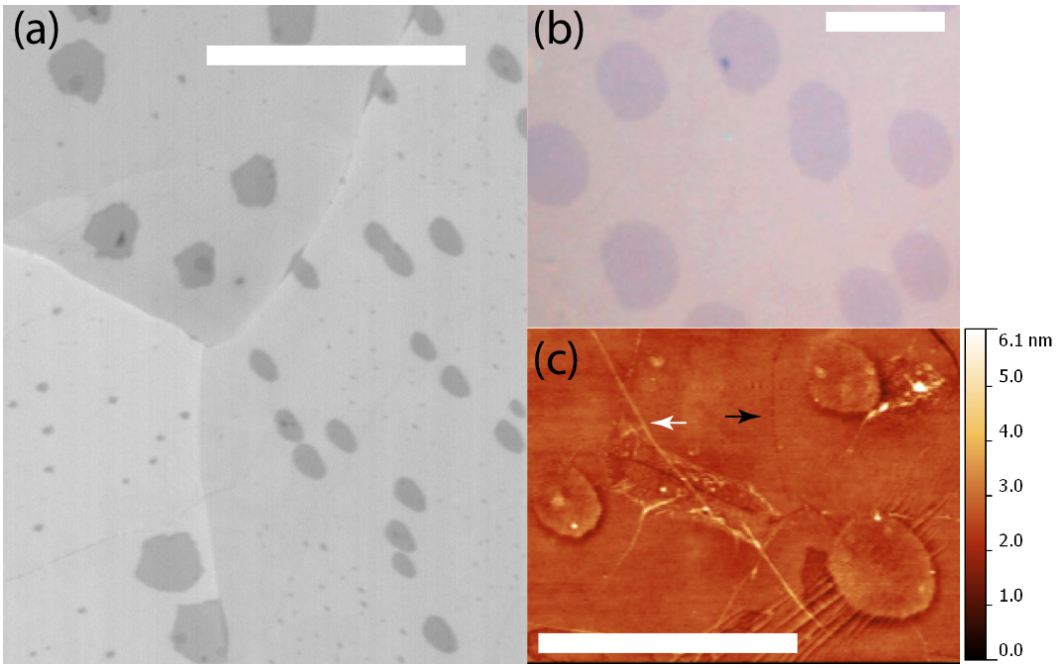


Figure 3.1: Scanning electron micrograph (a), optical micrograph (b), and atomic force micrograph (c) of graphene grown by ambient-pressure chemical vapor deposition on Pt foil. Image (a) is as-grown sample on Pt foil; the scale bar is 5 $\mu$m. The three large areas of different contrast are three crystalline grains of the Pt foil. Image (b) is taken after transfer of graphene to $SiO_2$/Si substrate; the scale bar is 10 $\mu$m. Image (c) is taken on graphene on poly methylmethacrylate transfer layer transferred upside-down to $SiO_2$/Si. The scale bar is 5 $\mu$m. Raised and lowered wrinkles are indicated by white and black arrows, respectively. In all cases few-micron-sized islands of different contrast are evident.

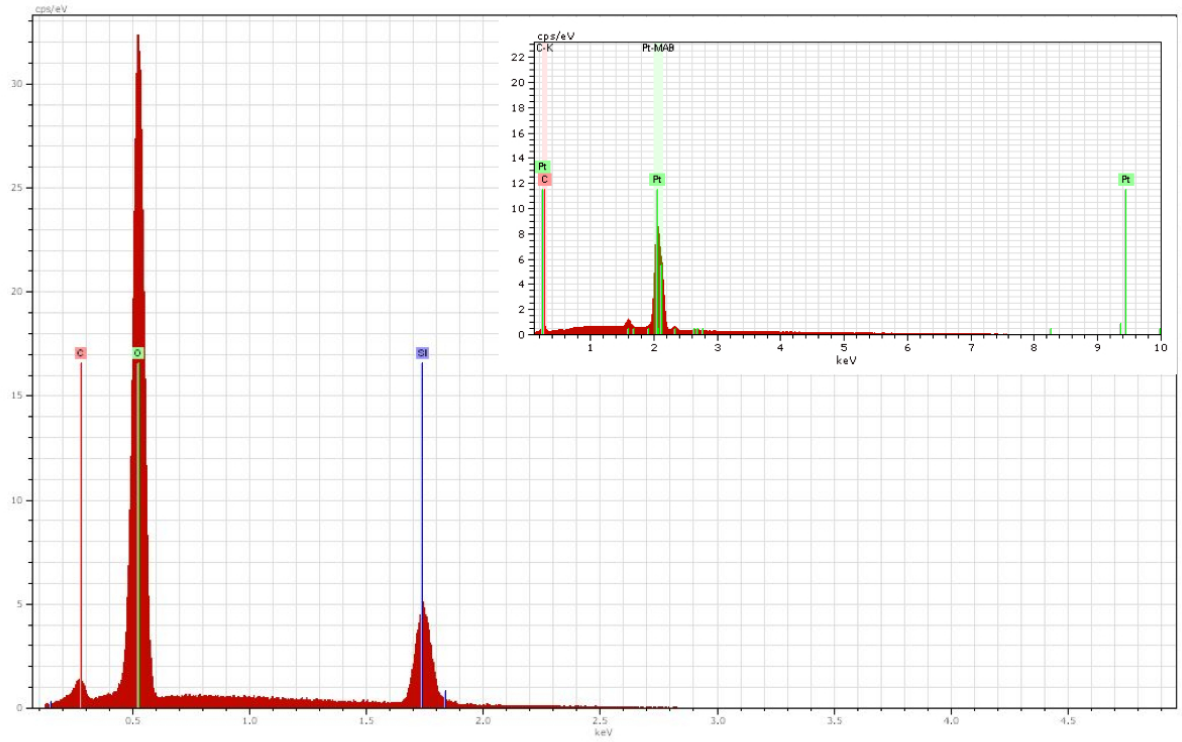


Spectrum: 1493

| El | AN | Series | unn. C [wt.%] | norm. C [wt.%] | Atom. C [at.%] | Error [%] |
|---|---|---|---|---|---|---|
| C | 6 | K-series | 1.85 | 1.10 | 1.76 | 0.4 |
| O | 8 | K-series | 100.81 | 60.19 | 71.90 | 11.3 |
| Si | 14 | K-series | 64.84 | 38.71 | 26.34 | 5.2 |
| | | Total: | 167.50 | 100.00 | 100.00 | |

Figure 3.2: EDX detects carbon, silicon and oxygen for a transferred graphene sample on $SiO_2$. The inset shows EDX for pre-transferred graphene on Pt. Only carbon and substrate elements are detected in both cases.

## 3.2 Orientation Dependence of Impurities

We identify the orientations of monocrystal Pt via EBSD and image the island layers grown on corresponding Pt grains via SEM. Crystalline orientations can be compeletely described by either the combination of plane direction and crystal direction {h k l}<u v w> or Euler angles ($\phi_1$, $\Phi$, $\phi_2$). Index {h k l} represents atomic arrangements on the cleavage surface, the last Euler angle, $\phi_2$, represents rotation of the crystal in the plane of cleavage surface with respect to the reference direction (RD), provided that Bunges (passive) description is used. As an example given in Figure 3.3, maps of inverse pole figure (IPF), Figure 3.3(b), and Euler angles, Figure 3.3(c), are shown for three monocrystals A, B, and C as in Figure 3.3(a). Given {h k l} and $\phi_2$, we obtain the top-view of the crystals shown in Figure 3.3(g)-(i). We define a direction in the cleavage face along the most exposed atoms on the top layer, representing the anisotropy of this facet. We found that the defined direction coincides with the longitudinal axis of the impurity layers, if there is one. For cleavage faces lacking such an axis, as in case A of Figure 3.3(d), the impurity layers do not show obvious anisotropy. Thus the anisotropy of the crystal face does relate with that of the morphology of the impurity layers. This relationship holds for about 50 grains on the sample that have been scanned.

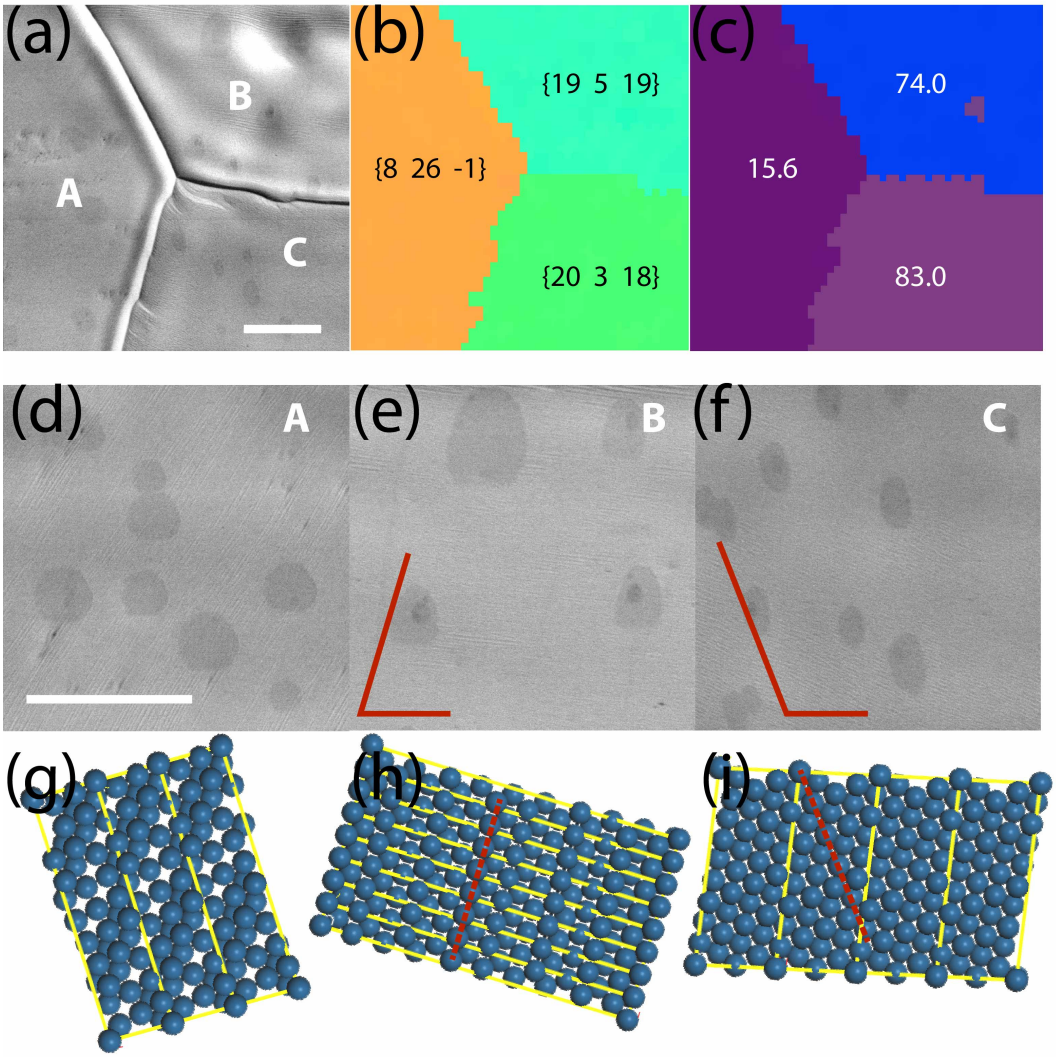


Figure 3.3: The SEM image (a) shows platinum substrate with 3 grains A, B, and C of different orientations, whose IPF map and Euler angles map are shown in (b) and (c). The plane direction {h k l} and the last Euler angle $\phi_2$ are shown in the corresponding map. The atomic arrangements are shown respectively in (g), (h), and (i) below detailed SEM images in (d), (e), and (f) marked with directions, if exist, defined in the text. The angles formed by the axes and the RD are also shown in the SEM images to guide eyes. The scale bars in (a) and (d) are 5 $\mu$m.

It is important to understand whether the impurity carbon is deposited on top of the monolayer graphene or forms underneath. Our EBSD results show a strong correlation between the anisotropy of the impurity islands and the crystalline orientation of the Pt substrate (Figure 3.3), but not the crystalline orientation of the graphene which is continuous across many Pt grains. The correlation strongly suggests that the impurity islands form beneath the monolayer graphene at the Pt surface; given that the islands are not highly crystalline themselves the anisotropy probably results from anisotropic diffusion of carbon along the Pt. The detailed mechanism of the carbon cluster formation calls for further theoretical investigation[44, 45]. However all results confirm the growth-from-below model for graphene on Pt[46].

## 3.3 Characterization of Impurity Decorated Sample by Dark Field TEM Technique

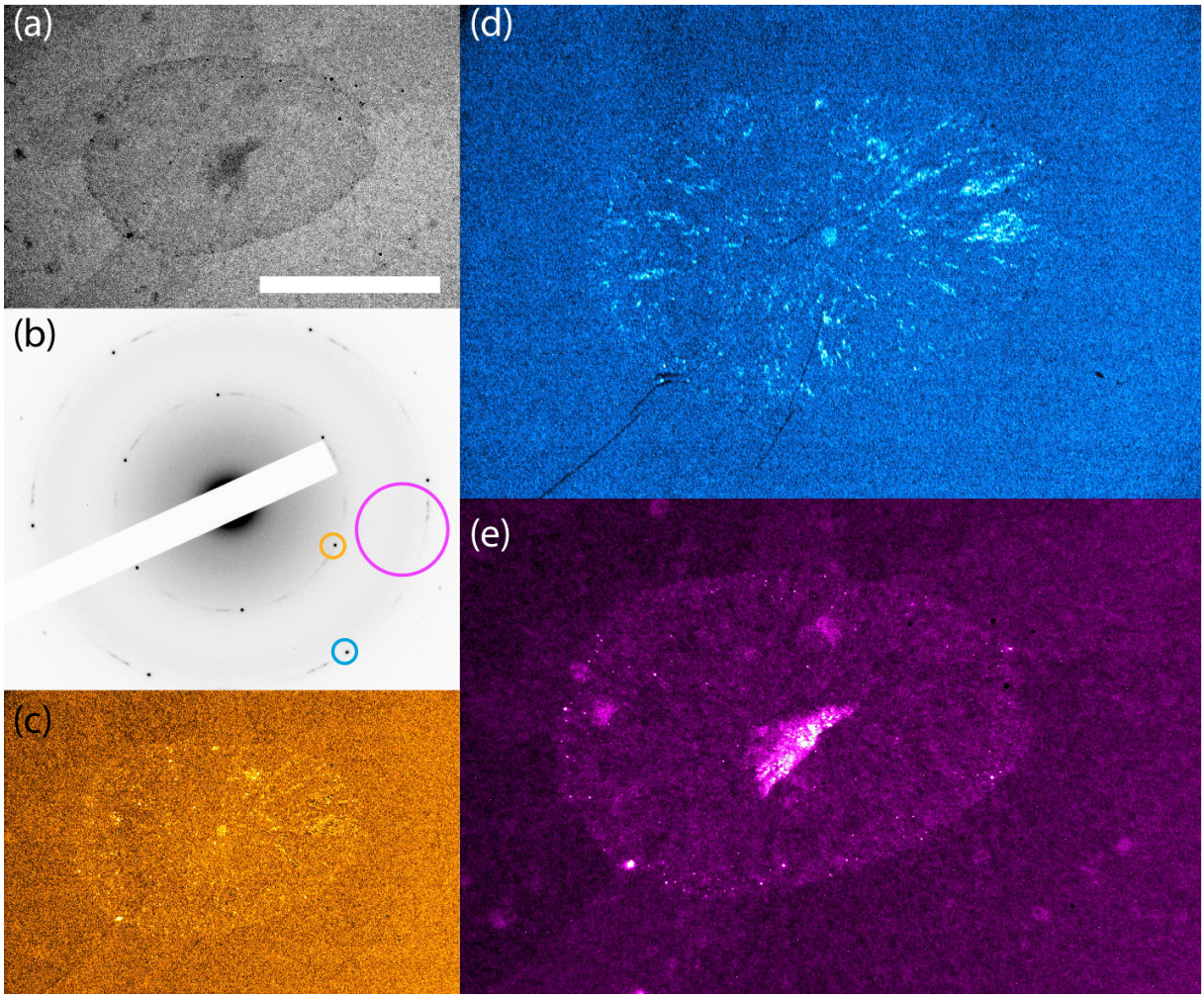


Figure 3.4: Transmission electron microscopy and diffraction of Pt-grown graphene. (a) Bright field image with scale bar of 1 $\mu$m. (b) Electron diffraction pattern corresponding to sample in (a). (c-e) Dark field images corresponding to orange (c), blue (d) and magenta (e) apertures indicated in (b).

Dark field TEM technique as an efficient characterization method of graphene is discussed in Chapter 2. To investigate the structure of the impurity decorated

samples via TEM, I transferred them onto 10 nm thick silicon nitride membranes. Figure 3.4(a) is a bright-field TEM image of the sample showing an island similar to those seen in Figure 3.1. Figure 3.4(b) shows the corresponding electron diffraction pattern. The diffraction pattern contains (1) bright main spots corresponding to monolayer graphene (2) a diffuse background from the amorphous $Si_3N_4$ membrane, and (3) sharp rings at the same radius as the monolayer graphene spots, with varying intensity along the rings, including some discrete spots. The pattern of intensity variation along the first-order and second-order rings has six-fold symmetry; the wave vector and symmetry of the sharp rings is entirely consistent with graphene indicating that the rings originate from crystalline graphitic carbon. Note that the possibility of the existence of additional carbon adatoms or/and nano-size isolated amorphous carbon cannot be excluded as these would be difficult to detect in diffraction. Dark field images of the first-order (Figure 3.4(c)) and second-order (Figure 3.4(d)) graphene diffraction spots are fairly uniform indicating that a monolayer of graphene corresponding to the main diffraction spots covers the whole image area. The second-order dark field image (Figure 3.4(d)) demonstrates that overwhelming majority of the additional material in the island region does not share the same orientation with the background monolayer graphene, though there are minority parts with a radial configuration and sizes ranging from nm to 100 nm that do align with the continuous monolayer. The observation of the impurities on my sample is in contrast with bilayer graphene impurities in graphene grown on Cu[46], Ni[47, 48] and Fe[49], and hardly Raman-detectable due to their small sizes.

Figure 3.4(e) shows an additional dark-field TEM image, with a larger aper-

ture to include many diffraction spots on the sharp second-order ring. Here dark field TEM shows bright domains distributing throughout the whole surface inhomogeneously. The correspondence between the dark region in the bright field image Figure 3.4(a) and bright region in the dark field image Figure 3.4(d) and (e) confirms that the bright domains in Figure 3.4(d) and (e) mainly represent carbon impurities as an additional layer instead of crystalline defects in the continuous monolayer. This is the major finding of this chapter: nanocrystalline graphene, misoriented with respect to the continuous monolayer graphene, exists across the entire sample. The impurity graphene is inhomogeneously distributed, with a higher concentration in few-micron-sized island regions, but concentrations also detected outside the islands. This is consistent with what we observed by optical microscope and AFM and further verified with high resolution TEM (HRTEM) as in Figure 3.5.

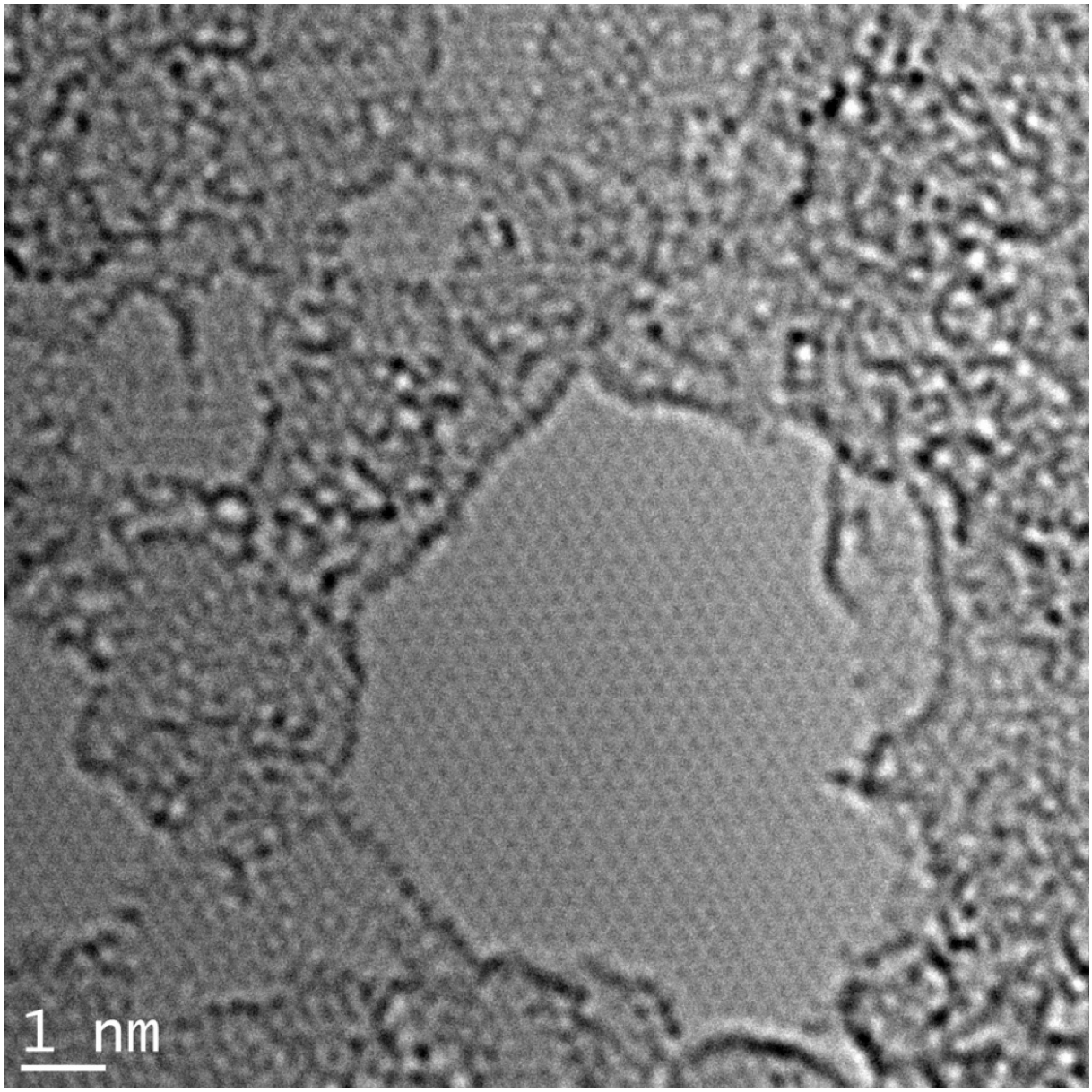


Figure 3.5: HRTEM image of graphene sample synthesized via CVD on Pt, which shows the background monolayer graphene and nanocrystalline impurities.

## 3.4 Characterization by Raman Spectroscopy and Electronic Transport Measurement

We now turn to Raman spectroscopy of our Pt-grown graphene samples, using a 633 nm laser excitation source and a confocal microscope to map the Raman spectra at the submicron scale. Figure 3.6(inset) shows a typical Raman spectrum of graphene grown on Pt similar to those examined in Figure 3.1 and 3.4 and a reference sample grown on copper (with reduced carbon impurities as seen in TEM). It is immediately evident that the Raman spectrum for the Pt-grown graphene with carbon impurities is distinct from that reported for exfoliated graphene[29] or Cu-grown CVD graphene shown here or reported before[15]. The Pt-grown graphene exhibits a pronounced and extremely wide D peak and broad wings to the G peak. The spectrum could be consistent with the superposition of a graphene spectrum (with sharp G and 2D peaks) with a spectrum of nanocrystalline graphitic carbon (with very broad D and G peaks, and similar G and D intensities). The $I_D$:$I_G$ ratio attributed to the nanocrystalline graphene is about 1:1, corresponding to a grain size of order 10 nm[43]. The main panels of Figure 3.6(a) show the G and 2D peaks in greater detail. Excepting the broad background, the G peak of the impurity-decorated sample is similar in width, but slightly upshifted in position, compared to those of the Cu-grown sample (and typical exfoliated graphene samples). The impurity-decorated sample also shows a somewhat broader, upshifted, but still Lorentzian 2D peak.

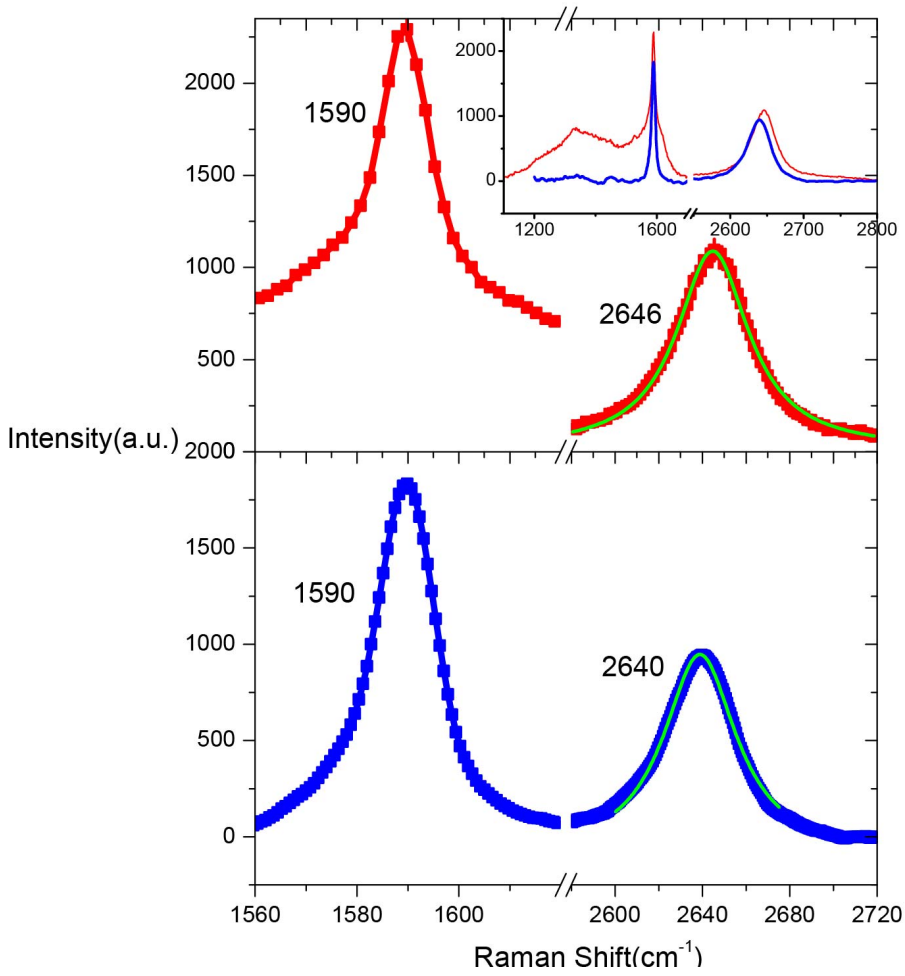


Figure 3.6: Raman spectroscopy and electrical characterization of Pt-grown graphene with impurities similar to Figures 3.1 and 3.4 is shown in red, and for comparison Raman spectrum from a Cu-grown graphene sample without impurity regions is shown in blue. Inset shows full spectra while main panel shows the G and 2D peak regions, with peak positions in wavenumbers ($cm^{-1}$). Lorentzian fits to the 2D peaks are shown in green.

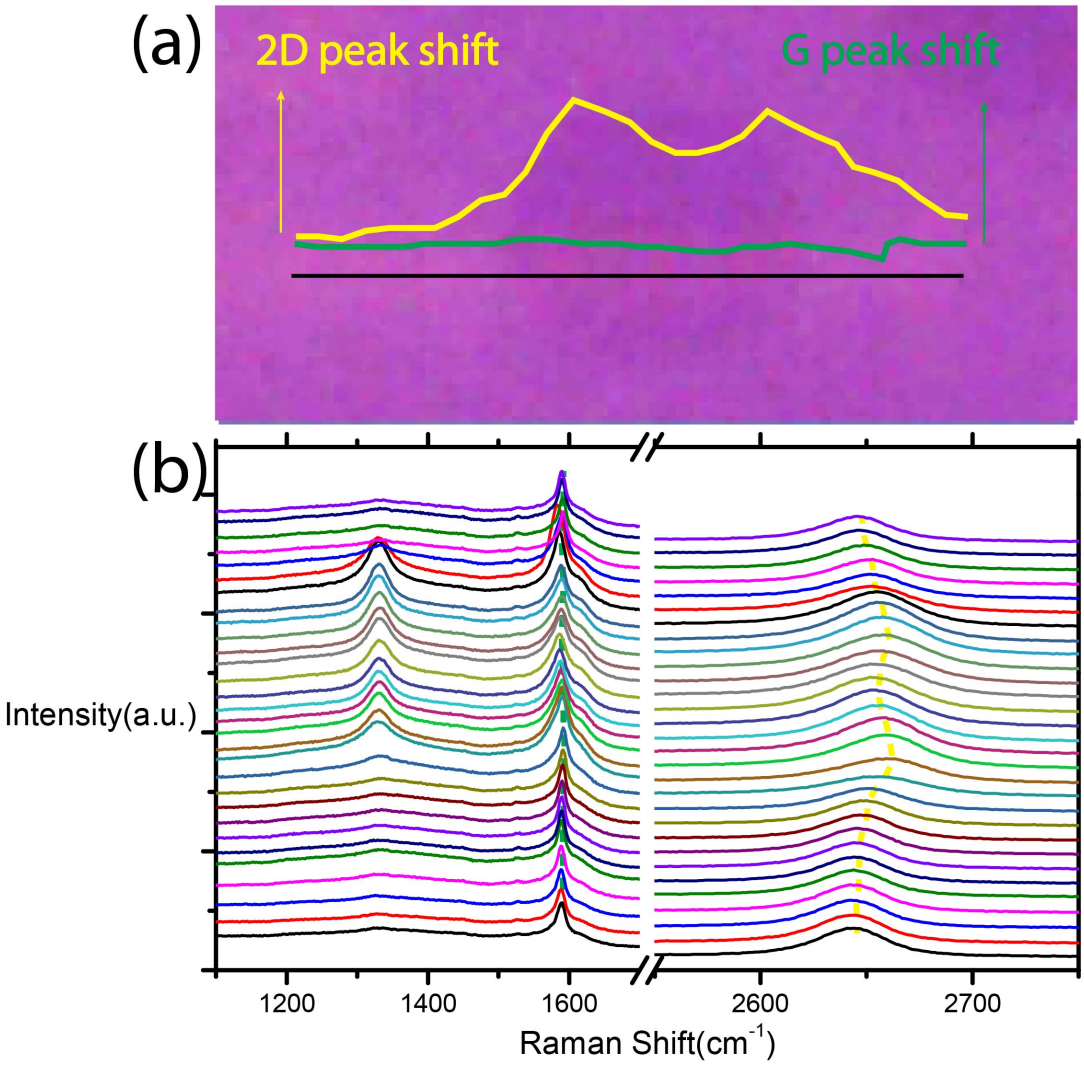


Figure 3.7: Raman spectra (b) of Pt-grown graphene taken at points with spacing of 0.31 $\mu$m along the 9 $\mu$m long black segment in the optical image (a). The position or blueshift of the 2D peak is extracted from Raman spectra and projected onto the real-position optical image. The length of the yellow and green arrows in (a) is 15.32 $cm^{-1}$. Note that the maximum blueshift happens inside the edge of the island due to $\mu$m resolution of Raman microscopy.

Figure 3.7 (b) shows Raman spectra of the impurity-decorated Pt-grown graphene

taken along a line crossing an impurity island as shown in the optical image (a). Raman spectra both on the island and off show the broad background in the D and G peak regions, indicating nanocrystalline graphitic carbon. The 2D peak remains Lorentzian everywhere, showing no evidence of large-sized Bernal-stacked graphite. An upshift of the 2D peak is associated with the island region, while the G peak is hardly changed in width or position. The consistency of the G peak excludes doping as the cause of the changes observed in the 2D peak[50]. Instead, the blueshift of 2D peak is in consistent with what was observed in turbostratic graphene[51, 21] supporting our identification of the impurity carbon as graphitic but largely mis-aligned with the continuous monolayer graphene.

Figure 3.8 shows the electrical conductivity as a function of back-gate voltage of the impurity-decorated Pt-grown graphene transferred to a $SiO_2$/Si substrate. The field effect mobility at 4.2 K and room temperature(RT) is about 6000 $cm^2V^{-1}s^{-1}$, comparable to other graphene samples obtained by CVD[15, 52] showing much lower D peaks in Raman spectra. Again this is indicative that the D peak in our samples arises from defects in the carbon impurity layer, not in the continuous monolayer. We also explored the conductivity of a Hall bar region from which the impurity islands were excluded by etching and found only a slight mobility change in the blue curve of Figure 3.8 indicating that the impurity island regions are not entirely responsible for the decreased mobility compared to exfoliated graphene on $SiO_2$[2, 53]. The Hall bar is an ideal geometry for Hall effect measurement[54]. As shown in the inset of Figure 3.8, constant current is applied between leads a and b. The transverse resistance is measured between each pair of A, B and C or A, B,

and C. The Hall resistance is measured between AA, BB, or CC. Such four-probe geometry decouples the resistance of the sample from that of the contacts between sample and leads.

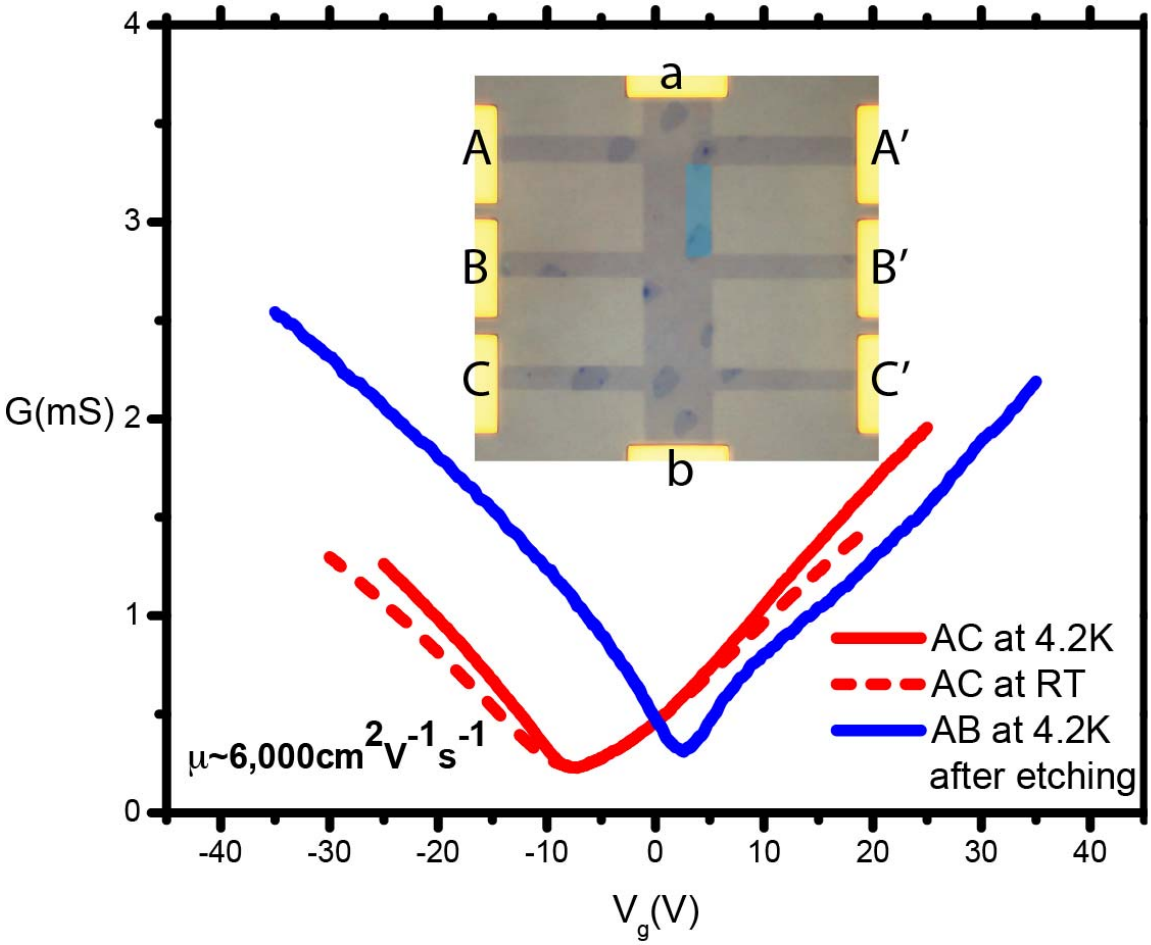


Figure 3.8: Conductivity as a function of back gate voltage for a Pt-grown graphene sample with impurities on 300 nm $SiO_2$/Si substrate. An image of the Hall bar device is shown in the inset; the top and bottom electrodes a and b are used as the source and sink current. The width of the Hall bar is 10 $\mu$m.

Amorphous carbon impurity islands can be easily mistaken for multi-layer re-

gions in optical images. The Raman spectra of our sample shows a very large and broad D feature normally associated with highly defected carbon[43]. Here we have associated the enhancement of the D peak with carbon impurities; the high electronic quality of our sample excludes the possibility that the defects responsible for the D band are in the continuous monolayer graphene[43]. Therefore the work demonstrates the importance of characterization by TEM for reports of new synthesis methods for graphene, since it gives the most accurate crystalline information.

# Chapter 4

# MAGNETO-TRANSPORT OF IMPURITY DECORATED GRAPHENE

My discovery of nanocrystalline carbon impurities with TEM techniques is discussed in the preceding chapter. I found that the impurities not only concentrate in island-like regions but also distribute sparsely under monolayer graphene. Such inhomogeneous impurity decorated sample indicates inhomogeneity may lead to trivial electron-transport property, as shown by the conductance curve of Figure 3.6 in Chapter 3, since the electrical field **E** is always perpendicular to the current **J**. The application of magnetic field, however, introduces bias in the transverse direction of the sample, the Hall effect, that reveals more about the transport properties, such as mobility, effective mass, scattering rate, magnetoresistance, etc. of the system.

Magnetoresistance (MR), the change of resistance of a material in a magnetic field, has long been of interest for both fundamental understanding of electronic conduction, and applications such as magnetic memory[55]. Resistivity is symmetric in $B$, and hence the leading correction to the resistivity $\rho(B) - \rho(0)$ is typically quadratic in $B$ and such quadratic MR is understood as a classical phenomenon. A long-standing theoretical quandary then has been the explanation of linear MR (i.e. $\rho(B) - \rho(0)$ is linear in $B$) in certain materials. The consensus is that linear MR arises from one of two mechanisms[56]: (1) in small bandgap materials with very

high mobility, a quantum linear MR arises when the Fermi energy lies in a partially-filled Landau level[57, 58] while (2) in highly spatially inhomogeneous materials linear MR can also arise.

In this chapter I present transport and magneto-transport measurements of chemical-vapor-deposited graphene samples with different degrees of inhomogeneity induced by controlling the amount of nanocrystalline graphitic impurities. I find that the charge carrier inhomogeneity in graphene, characterized by the width of the minimum conductivity region $n^*$, is positively correlated with the density of graphitic impurities on the graphene, and cannot be explained by variation in charged impurity density alone. I examine the low-field quadratic MR as a function of carrier density $n$. I find that the quadratic MR is a universal function of $n/n^*$ for all the samples studied here, and an additional exfoliated sample from Ref.[6]. The scaling suggests that the MR arises from a classical mechanism due to carrier-density inhomogeneity, though a theory for MR in an inhomogeneous medium at finite carrier density is lacking. In the most inhomogeneous samples the MR near the Dirac point is strikingly linear. I exclude the possibility that the linearity reflects Abrikosov's quantum MR, and instead relate the magnitude and linearity of the MR with inhomogeneity. I find a phenomenological three-parameter equation to describe the linear and quadratic MR near the Dirac point in all samples as a universal function of n/n*, again suggesting that the magnetoresistance is driven by inhomogeneity.

## 4.1 Normal Transport and Magneto-transport Properties of Impurity Decorated Graphene

In Figure 3.8 of Chapter 3, the conductivity of as-grown impurity decorated graphene synthesized on Pt at 1000° C demonstrates a decent mobility of about 6000 $\mathrm{cm^2V^{-1}s^{-1}}$ unrelated to the island-like impurity layers. We call this sample as Sample 1. The conductivity of Sample 1 is linear over a large range of carrier density, $\sigma \propto n$, as a consequence of charged impurity scattering[59, 60]. The mean-free-path $\lambda$ of mesoscopic-size device made from Sample 1 depends on conductivity $\sigma$ as

$$\lambda(n) = \frac{\sigma}{2e^2/h}\frac{1}{2\sqrt{n/\pi}}, \tag{4.1}$$

where $e$ is the charge of an electron, $h$ is the Planck constant and $n$ is the carrier density relating to Fermi energy $\epsilon_F$ as

$$n \approx \frac{1}{\pi}\left(\frac{\epsilon_F}{\hbar v_F}\right)^2, \tag{4.2}$$

where $\hbar$ is the reduced Planck constant and $v_F$ is the Fermi velocity. The mean-free-path shown in Figure 4.1 increases linearly beyond the Dirac point.

The divergence of the mean-free-path near the Dirac point is contrary to the finite conductivity at the Dirac point that was observed. The reason is the notorious spontaneous electron-hole puddles of graphene near the Dirac point[31, 32], limiting the mean-free-path to the scale of the fluctuation. Since electrons and holes in graphene obey Dirac quantum mechanics as in Section 1.2 of Chapter 1, there are certain possibilities that charge carriers penetrate through barriers and contribute to the overall conductivity[11], breaking the Anderson localization[61]. The range of

the carrier density in which the conductivity is governed by this electron-hole puddle is estimated by $n^* = \sigma_{\min}/e\mu$[62, 63, 64] where $\sigma_{\min}$ is the minimum carrier density and $\mu$ is the mobility. Using Equation 4.1 and 4.2, we obtain the inhomogeneity-dominated range of Fermi energy $\epsilon_F^*$ as indicated in Figure 4.1.

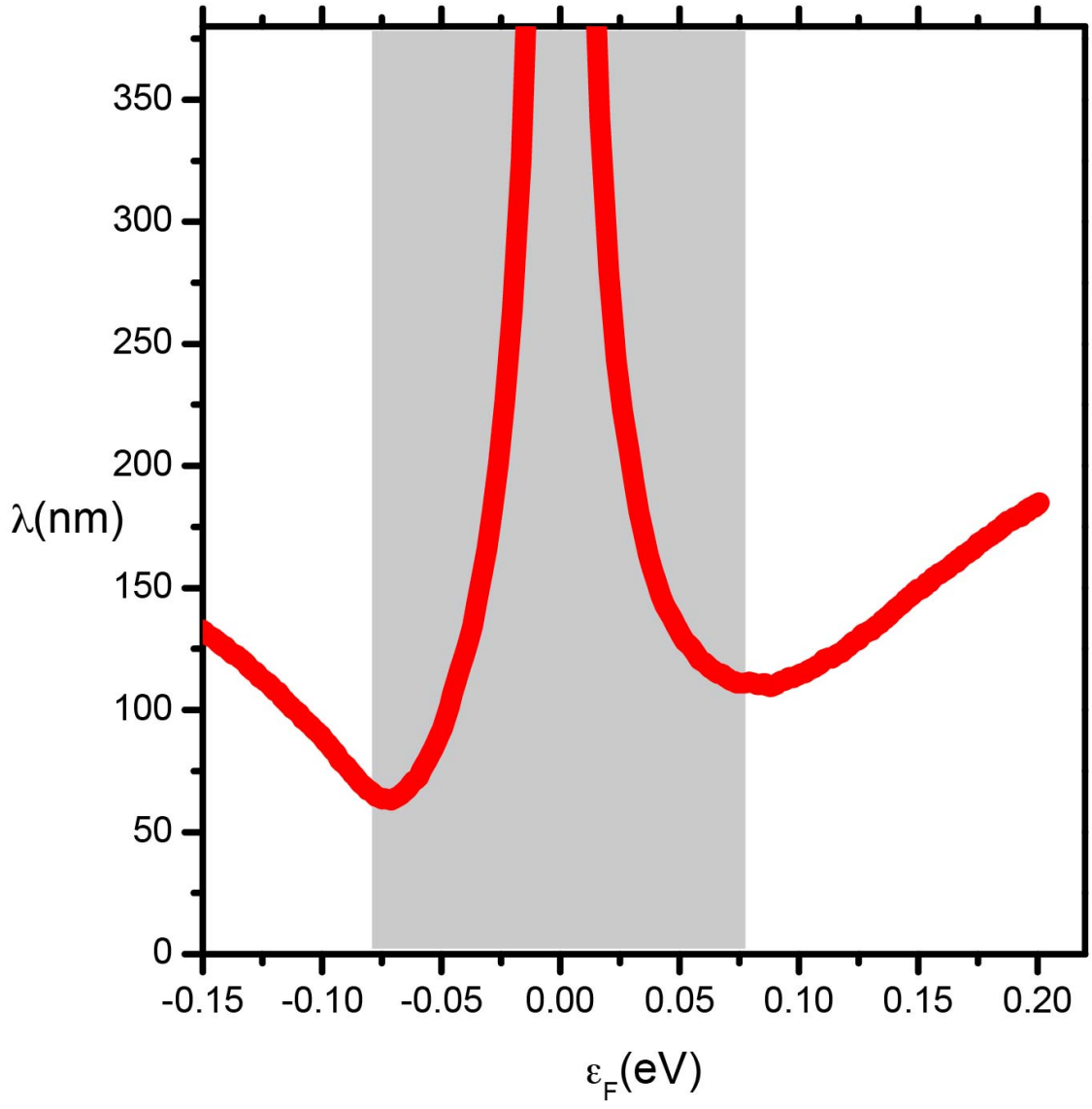


Figure 4.1: The estimated mean free path of Sample 1 is shown with the shadow region covers the range between $-\epsilon_F^*$ and $\epsilon_F^*$.

We write the total conductivity as[59, 62, 63, 65, 66, 67]

$$\sigma = \sigma_{\text{res}} + Ce\left|\frac{n}{n_{\text{imp}}}\right|, \tag{4.3}$$

where $C$ is a constant and $\sigma_{\text{res}}$ is the residual conductivity at $n = 0$. The residual conductivity for Sample 1 is $\sim 0.25$ mS as indicated in Figure 3.8.

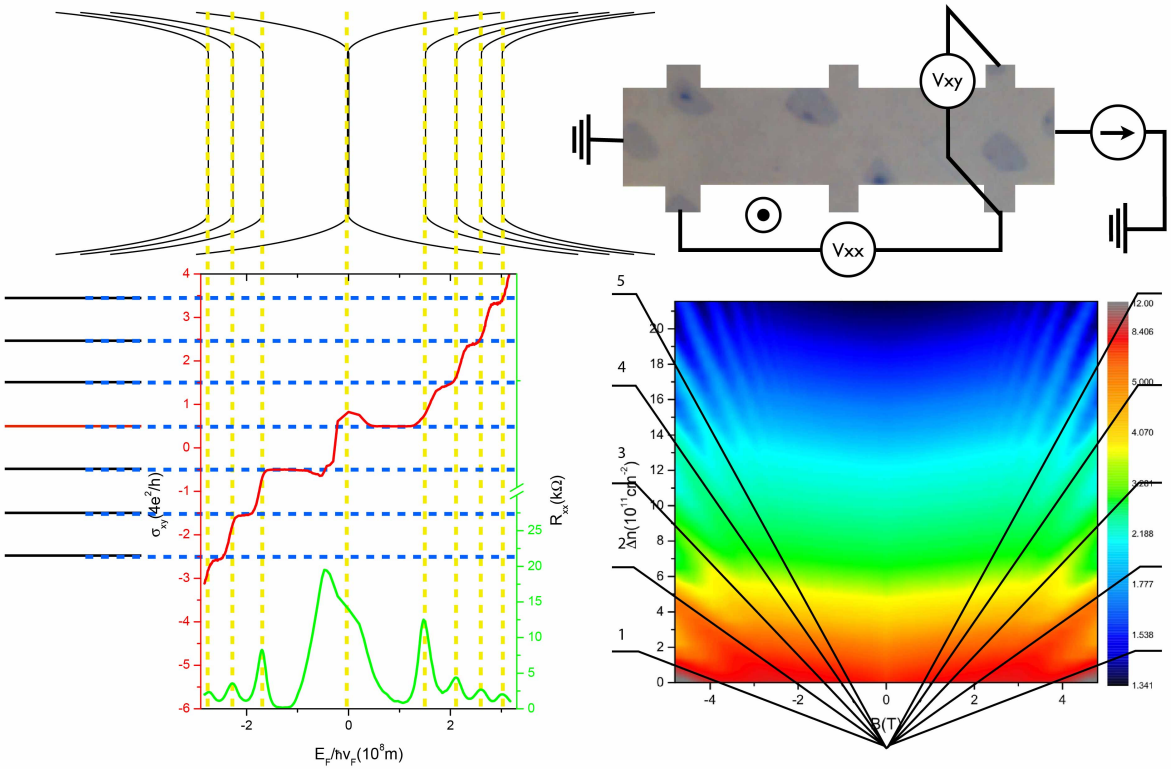


Figure 4.2: Transverse resistance shows Shubnikov-de Hass oscillations at Fermi levels described by Equation 4.5. The Hall conductivity indicates plateaus according to Equation 4.4. $N = 1$ to 5 is shown in the Landau Fan below the device configuration.

More properties of Sample 1 can be understood by applying a magnetic field[68]. The classical Hall effect in graphene can be well interpreted by Boltzmann transport theory as explained in Appendix B. The quantum Hall conductivity indicates

plateaus due to[69, 70]

$$\sigma_{xy} = \pm 4(N + 1/2)\frac{e^2}{h}, \tag{4.4}$$

where $N = 0, \pm 1 \pm 2, \cdots$ is the quantum number corresponding to blue dashed lines in Figure 4.2 and $1/2$ corresponding to red energy level arises from the specific Berry phase $\pi$ of graphene[69] due to the zero effective carrier mass near the Dirac point[71]. The Landau level, indicated by yellow dashed lines, is described by[69, 70]

$$E_N = \mathrm{sgn}(N) = \sqrt{2e\hbar v_F^2 N B}, \tag{4.5}$$

where $N = 0, \pm 1 \pm 2, \cdots$, generating the Shubnikov-de Hass oscillations. The Landau levels for $N > 1$ are related to the carrier density by[69, 70]

$$\frac{n}{B} = \frac{2eN}{\pi\hbar}, \tag{4.6}$$

resulting in the Landau fan shown in Figure 4.2.

## 4.2 Inhomogeneity Correlated Magnetoresistance

A homogeneous single-band two-dimensional conductor such as ideal (homogeneous) graphene exhibits no MR (linear or quadratic) within the classical Boltzmann transport framework. MR has been abundantly observed in graphene-related materials, such as exfoliated graphene[6], graphite[72, 73, 74] or epitaxial multilayer graphene[75]. For monolayer graphene at or near the charge neutral point, or Dirac point, for which the poorly-screened Coulomb potential of randomly-placed charges in the environment generates carrier-density inhomogeneity, i.e. the notorious electron-hole puddles[31, 32], the MR can be explained as a classical effect

within effective medium theory[6, 76]. In the case of equal areas of electron and hole puddles with equal mobility $\mu$, one expects

$$\frac{\rho(B) - \rho(0)}{\rho(0)} = \sqrt{1 - (\mu B)^2}, \tag{4.7}$$

which for $\mu B \gg 1$ is approximately linear. Such MR was observed previously in graphene near the Dirac point[6] but with small corrections to Equation 4.7 possibly due to asymmetry in electron/hole area or mobility. However, no detailed study of MR in graphene with varying degrees of inhomogeneity has been carried out. Linear MR observed in multilayer graphene epitaxial grown on SiC was explained by a quantum mechanical model[75], due to the robustness of MR from 2.2 K to room temperature. This claim, however, is not valid to graphene whose mobility is barely temperature dependent.

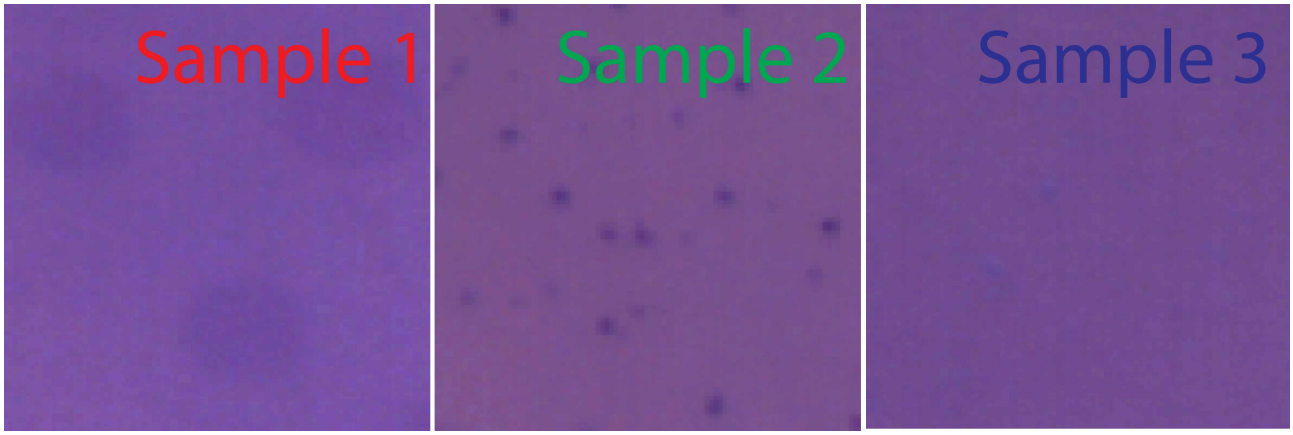


Figure 4.3: 10×10 $\mu$m optical images of Sample 1 to 3. Note the island-like impurities in Sample 1.

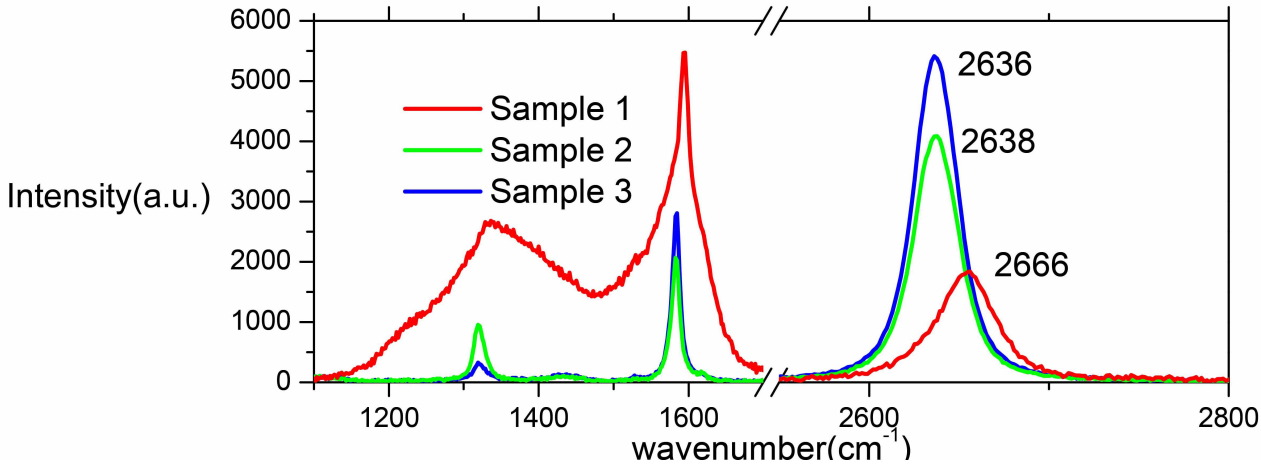


Figure 4.4: Raman spectroscopy with 633 nm laser.

The MR can be observed in Sample 1 in the Landau fan for $|B| \sim 2$ T as shown in Figure 4.2. Here I explore the MR in single-crystal monolayer graphene synthesized on Pt as described in previous chapters[35, 77]. I prepared graphene Samples 1 to 3, as in Figure 4.3, via CVD in flowing gas mixture of hydrogen and methane (5 sccm) on 20 $\mu$m thick Pt foil. For Sample 1, 2 and 3, temperature of 1000° C, 950° C, 900° C and hydrogen mass flow rate of 700 sccm, 500 sccm and 380 sccm respectively are used. The Raman spectrum of Sample 1 has a suppressed and red-shifted 2D peak, an enhanced D peak and an un-shifted G peak comparing to pristine graphene sample[77]. This trend in Raman spectroscopy is also built up through Sample 3 to 1 as in Figure 4.4. The implication is that Sample 1 has the greatest concentration of nanocrystalline carbon impurities, and Sample 3 the least.

Synthesized graphene is coated with PMMA with a spinning speed of 2000 rpm and transferred to a silicon dixoide wafer by the electrolysis method. The impurity layer was between the monolayer graphene and the substrate. Gold contacts

Table 4.1: Transport quantities of graphene samples synthesized on Pt with different inhomogeneity.

| Sample | $\sigma^*$(mS) | $\mu(\mathrm{cm^2V^{-1}s^{-1}})$ | $n^*(10^{11}\mathrm{cm^{-2}})$ |
|---|---|---|---|
| 1 | 0.276 | 6400 | 2.7 |
| 2 | 0.166 | 8200 | 1.3 |
| 3 | 0.205 | 11300 | 1.1 |

were evaporated onto single-crystal graphene which is then plasma-etched into a Hall-bar. All three devices share the same configuration as shown in the inset of Figure 4.5(a). The Dirac points are shifted to $V_g^{(0)} = 0$. From the conductivity curves in Figure 4.5(a), we extract the field-effect mobility $\mu$ and inhomogeneity density[62] $n^* = \sigma_{\mathrm{min}}/e\mu$ as in Table 4.1, indicating trends of enlargement of $\mu$ and reduction of $n^*$ from Sample 1 to 3. The mobilities are comparable with each other and relatively high for synthesized graphene with CVD method especially for Sample 3 to the level of exfoliated graphene. The variation in $n^*$ is somewhat greater (factor of 2.5) than would be expected from variation due to charged impurity density $n_{\mathrm{imp}}$ alone ($n_{\mathrm{imp}} \sim 1/\mu$ which varies by a factor of 1.8). The difference is particularly striking for Sample 1 and 2 with mobility differing by a factor of 1.3 while $n^*$ differs by a factor of 2.1. For Sample 1, there is a noticeable long range linearity of conductivity on the electron side due to charged-impurity scattering[59, 64, 65].

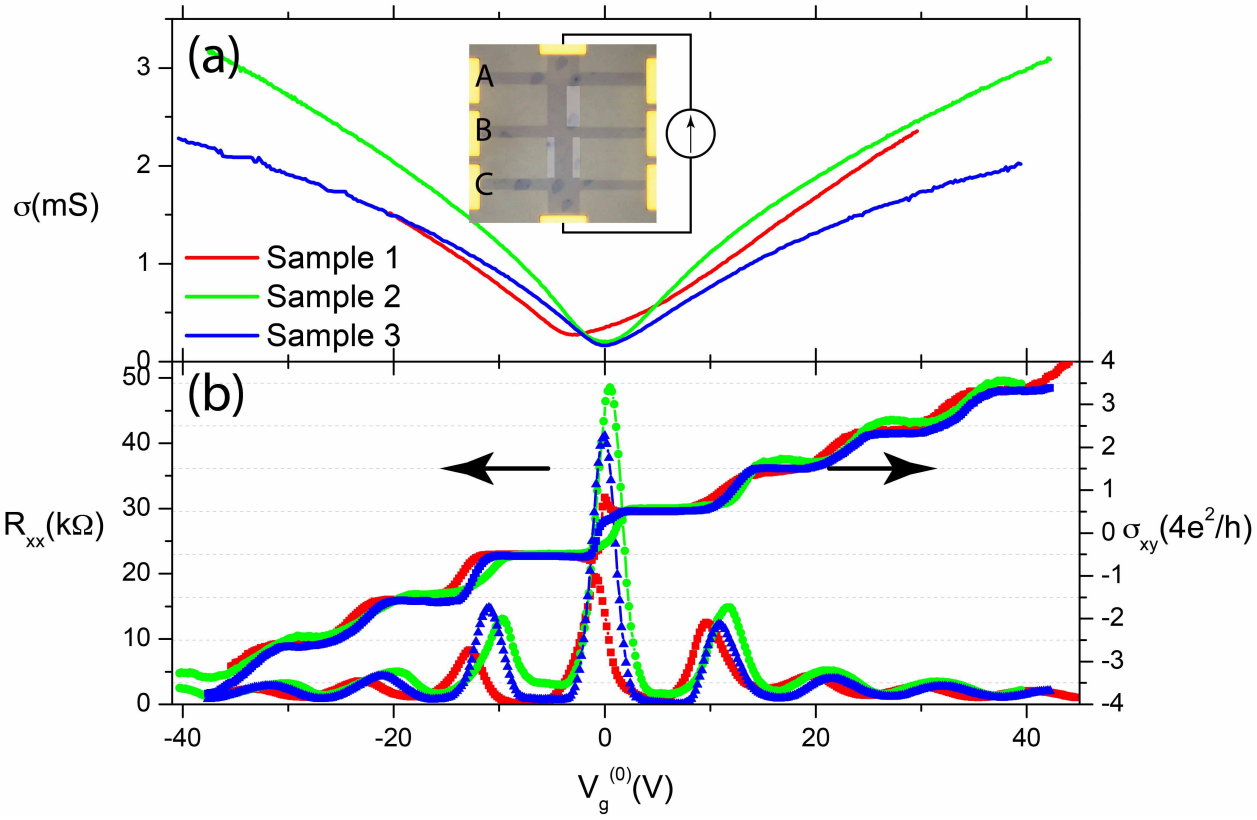


Figure 4.5: Conductivity at 4.2 K is shown in (a). Shadowed regions in the Hall bar device are etched afterwards to verify the influence of island-like impurities on MR. The width of the Hall bar is 10 $\mu$m. Transverse resistance and Hall resistance at 4.2 K under magnetic field of 8 T for all three samples are shown in (b).

The transverse resistance $R_{xx}$ and Hall conductivity $\sigma_{xy}$ of all three samples in Figure 4.5(b) demonstrate Subnikov-de Haas oscillations and plateaus and eventually quantized Hall conductivity plateaus with $\sigma_{xy} = 4(n + 1/2)e^2/h$ where the factor $1/2$ is the fingerprint of Berry's phase $\pi$ in monolayer graphene[70, 52] as in Section 4.1. Figure 4.6 shows the MR of Samples 1-3 at a few different gate voltages. Qualitatively one can see that the MR behavior shows differences among the three

samples. In particular Sample 1 clearly shows non-quadratic (and as I show below, quite linear) MR at small $V_g^{(0)}$. For comparable $V_g^{(0)}$ values both the magnitude and the functional form of the MR are different for different samples. Note for instance that at $V_g^{(0)} = 7$ V the zero-field resistance for Samples 1 and 2 are similar, but the MR in Sample 1 has a large magnitude and is linear, while the MR in Sample 2 shows smaller magnitude and is nearly quadratic. These differences are explored in detail below.

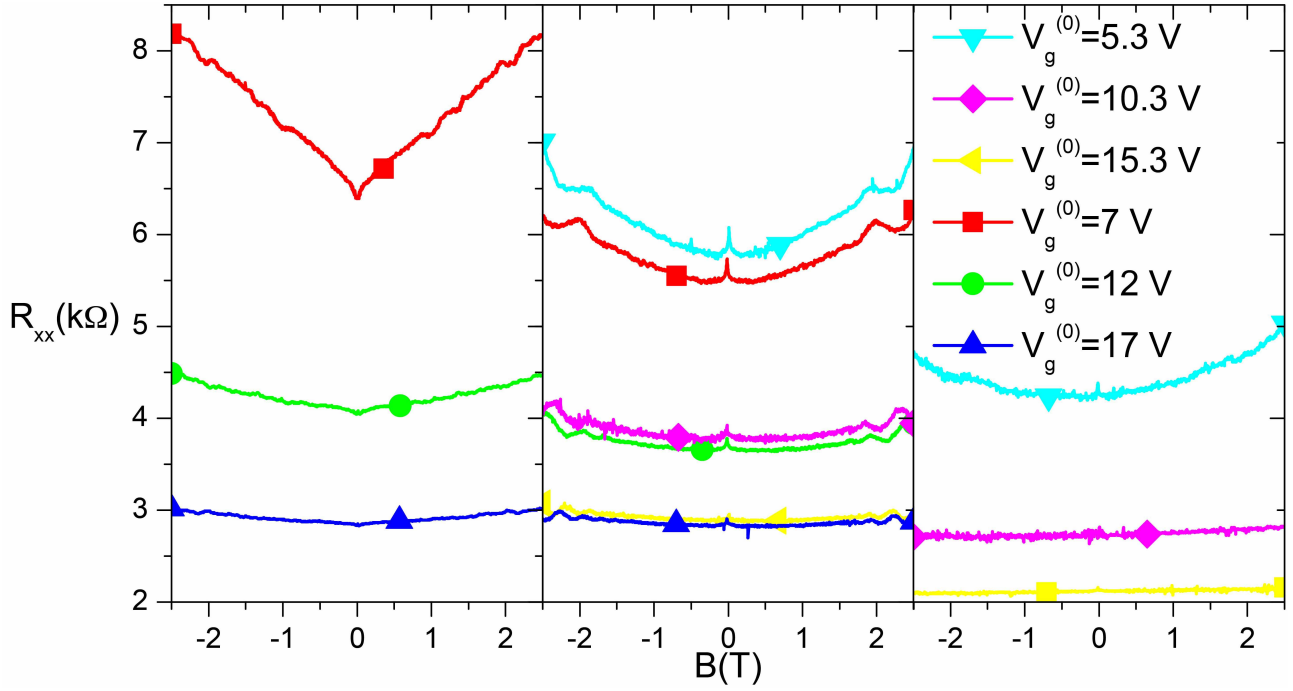


Figure 4.6: The MR at 4.2 K for Sample 1 to 3 from left to right is compared. The MR of the same gate voltage, or carrier density, shares the same color.

## 4.3 Phenomenological Investigation on the Magnetoresistance

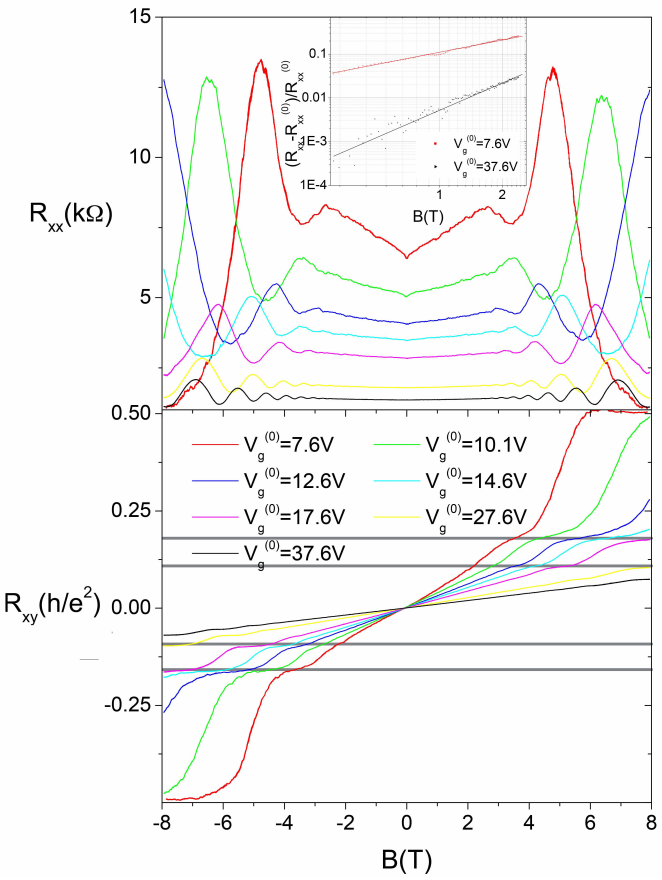


Figure 4.7: Transverse MR and Hall MR of Sample 1 are shown in top image and bottom image respectively at 4.2 K. The linearity and quadracity of MR at gate voltage of 7.6 V and 37.6 V is shown in the log-log plot of RMR, with fitted slopes of $0.95 \pm 0.05$ and $2.04 \pm 0.05$ respectively. Plateaus of Hall index 1/6, and 1/10 are marked out by grey lines.

I now discuss the MR and Hall effect in Sample 1 in detail. I find a region of low magnetic field where the Hall resistivity is linear in field (showing no correction due to Subnikov-de Haas oscillations, Figure 4.7(b)) but there is signifcant MR as seen in

Figure 4.7(a). Two features are noticed. (i) There is a transition from linear MR to quadratic MR as the carrier density increases. This is shown more clearly in the inset of Figure 4.7(a): a log-log plot of the MR vs. $B$ shows a slope of $\sim 1$ (linear MR) at carrier density $\sim 5.5 \times 10^{13}$ cm$^{-2}$ and slope of $\sim 2$ (quadratic MR) at $n \sim 2.7 \times 10^{12}$ cm$^{-2}$. (ii) The linear MR clearly exists for carriers densities beyond filling the first Landau level, as seen by the appearance of Shubnikov-de Haas oscillations at higher field for carrier densities where linear MR is observed. Feature (i) can not be explained by the quantum MR and feature (ii) disagrees with the extreme quantum condition of quantum MR that only one Landau level participates[57]. Thus we might expect that the linear MR in graphene samples produced by CVD on Pt and in that by epitaxial growth could be a result of inhomogeneity, a particularly enticing explanation as I have previously observed macroscopic inhomogeneity in the concentration of nanocrystalline graphitic impurities on these samples.

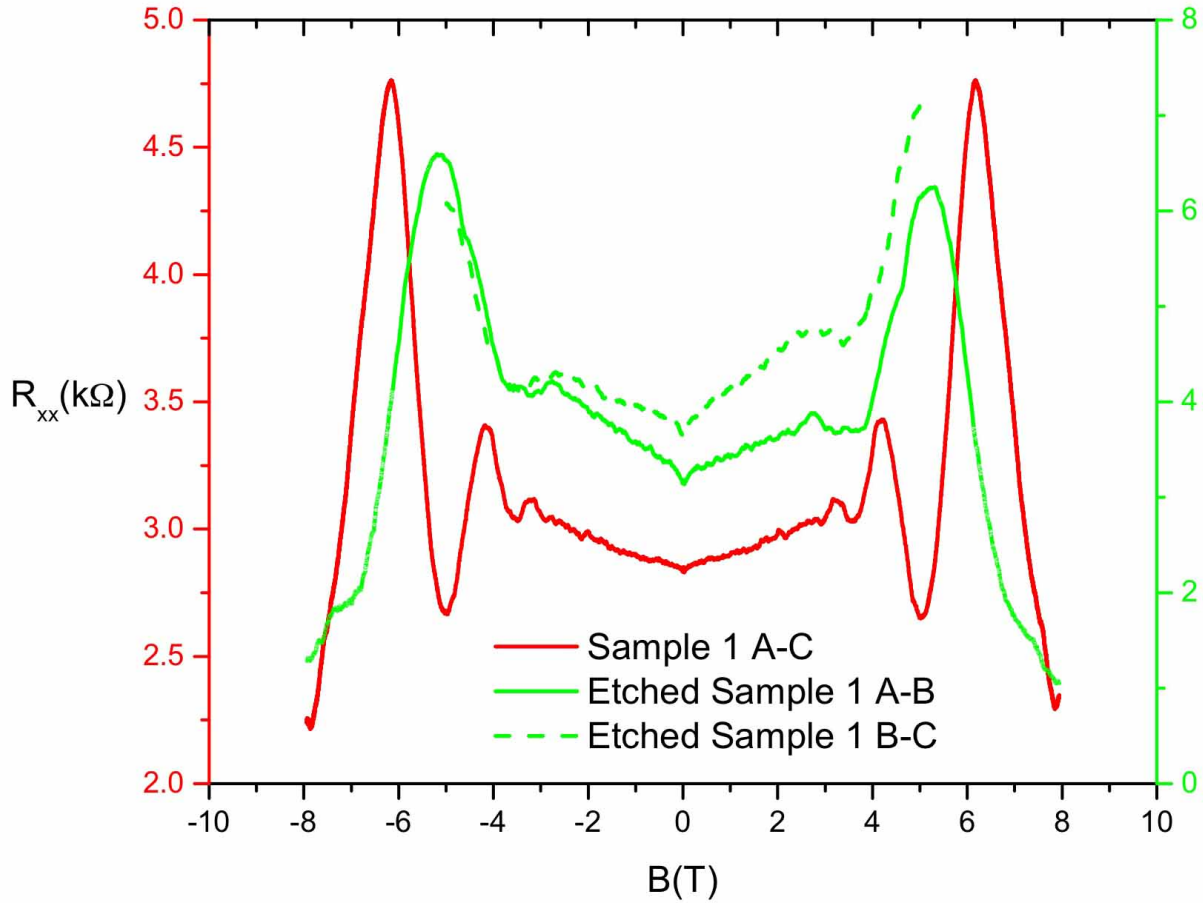


Figure 4.8: MR of pre- and post-etched Sample 1 at 4.2 K and gate voltage of 17.6 V.

I first checked whether the island-like structure of the impurities is responsible for the linear MR. I etched the island-like regions from the Hall bar of Sample 1 (see the inset of Figure 4.3(c)) but observed uneliminated MR after etching as shown in Figure 4.8. I therefore exclude island-like impurities as the origin of MR and instead turn to focus on the inhomogeneity induced by inhomogeneously distributed nanocrystalline carbon impurity under the monolayer graphene. The inhomogeneity results in inhomogeneous potential and thus electron-hole puddles[31, 32] and other networks of microscopic, such as NN or PP[78], junctions.

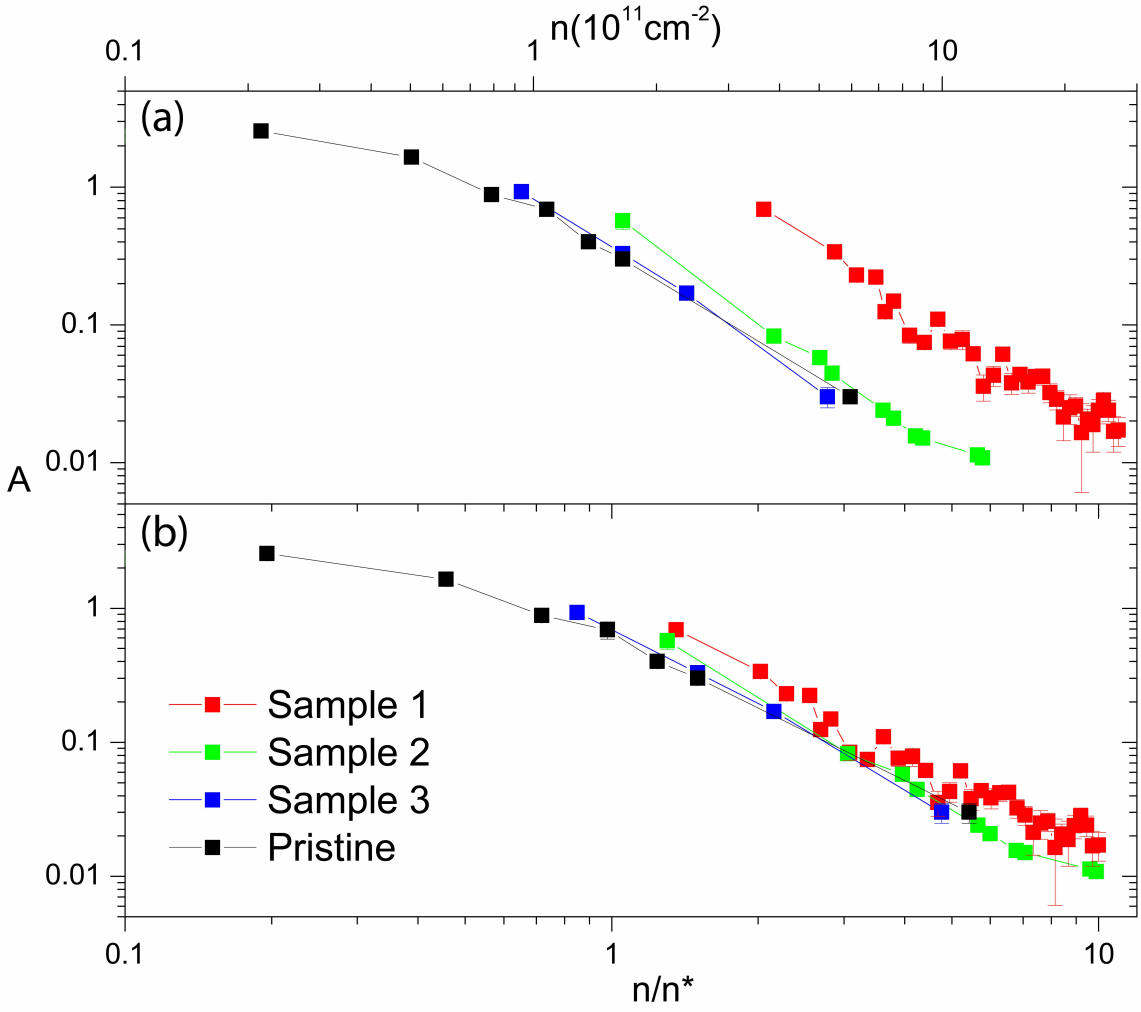


Figure 4.9: The log-log plot of unitless quantity $A$ with respect to the carrier density $n$ is shown in (a). Log-log plot of $A$ vs $n/n^*$ is shown in (b). The data for the Pristine sample are from published data of Fuhrer's group[6].

Before addressing the origin of the prominent linear MR in Sample 1, I explore the quadratic MR which is present in all samples at finite carrier density. The MR behaves quadraticaly in the low-field limit as $\left(\frac{\rho-\rho_0}{\rho_0}\right)_{\frac{\rho}{\rho_0}\to 0} = A\,(\mu B)^2$. Figure 4.9(a) shows the coefficient $A$ as a function of carrier density $n$ for Samples 1-3 as well as an additional exfoliated graphene sample (studied in Ref.[6]). There is a clear trend

of $A$ decreasing with $n$ for all samples, following roughly a power law $A \sim 1/n^2$. This is qualitatively consistent with inhomogeneity-induced MR: as the average carrier density increases, the size of the fluctuations relative to the average carrier density decreases, and increased free-carrier screening reduces the magnitude of the fluctuations as well. Thus one expects a strong suppression of MR at high carrier density, as observed.

If carrier-density inhomogeneity is driving the MR, I expect that the MR is determined by the parameter $n^*$. Since the coefficient $A$ is dimensionless, dimensional analysis argues that it should be a function of the only dimensionless parameter $n^*/n$ (Note that the Dirac band in graphene has no other characteristic length besides $k_F^{-1} \sim n^{-1/2}$; in particular there is no Bohr radius for Dirac electrons, and the screening length is proportional to $k_F$). Figure 4.9(b) shows $A$ with respect to $n^*/n$ and clearly demonstrates a collapse of data. Phenomenologically I find that at high carrier density $A = \alpha_1 \left(\frac{n^*}{n}\right)^{-2}$ with $\alpha_1 \approx 1$.

I extend the description of the MR closer to the Dirac point and to higher field by fitting to the following empirical formula inspired by the inhomogeneous effective medium theory (Equation 4.7)[6, 76]:

$$\rho_{xx}(B) = \left[\sigma_{xx} - \frac{\sigma_{\min}}{\alpha_2} + \frac{\sigma_{\min}/\alpha_2}{\sqrt{1 + \left(2\alpha_1\alpha_2\sigma_{\min}/\sigma_{xx}\right)(\mu B)^2}}\right]^{-1}. \tag{4.8}$$

The MR predicted by this equation with two unitless parameters, $\alpha_1$ and $\alpha_2$, has the same tendency of the observed MR: quadratic at low field, linear over a relatively large range of field and saturates at high field. This functional form was shown previously to give an excellent description of the MR near the Dirac point in exfoliated

graphene[6]. Equation 4.8 at the Dirac point ($\sigma_{xx} = \sigma_{\min}$) reduces to Equation 4.7 to within an adjustable parameter $\alpha_2$. Equation 4.8 also gives the correct value of $A = \alpha_1 \left(\frac{n^*}{n}\right)^{-2} \approx \alpha_1 \left(\frac{\sigma_{\min}}{\sigma}\right)^{-2}$ consistent with the findings above.

Figure 4.10(a) shows fits of the MR to Equation 4.8, which gives an excellent description of the deviations from quadratic MR over most of the range of carrier density for Samples 1-3. For Sample 1 at very low carrier density, the linear MR over a large range of magnetic field cannot be well-fitted. For Samples 2 and 3 at high carrier desnity the deviations from quadratic MR are very small, so there are large uncertainties in the parameter $\alpha_2$. All the fits in Figure 4.10(a) are performed in the magnetic field region of linear $R_{xx}$, and data near zero field (~0.2 T), where the weak anti-localization dominates[45, 79, 80], are excluded from the fits. The extracted $\alpha_2$ from the fitting as shown in Figure 4.10(b) has the order of unity for all three samples.

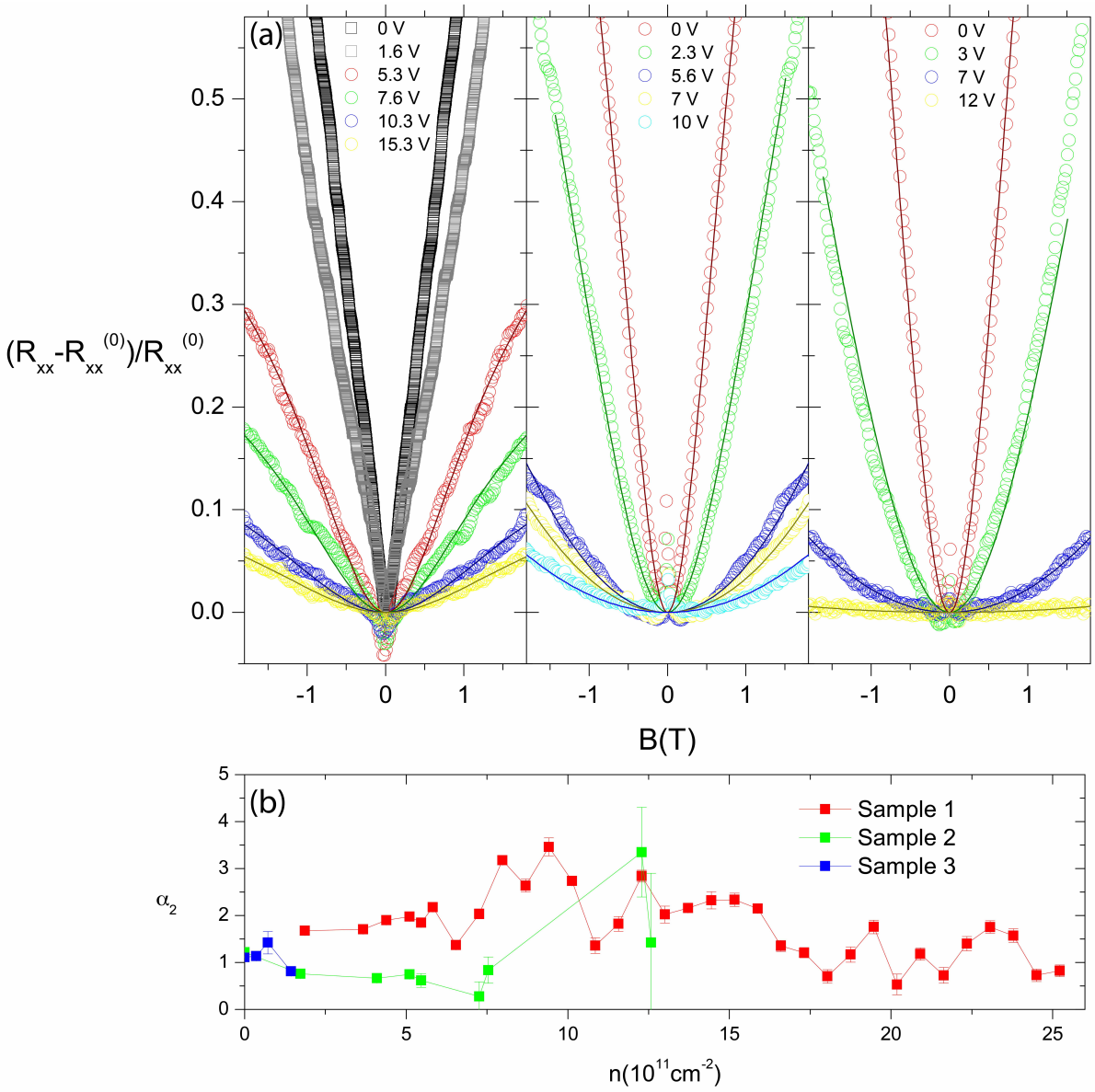


Figure 4.10: RMR of Sample 1 to 3 and fitted curves are shown in (a) from left to right. MR indicated by hollow squares(□) cannot be well-fitted by Equation 4.7. Fitted unitless parameter $\alpha_2$ is shown in (b).

## 4.4 Summery and Future Work

In summary, I have phenomenologically described the MR of graphene samples with varying degrees of inhomogeneity by a specific function of the inhomogeneity parameter $n/n^*$ (or conversely $\sigma/\sigma_{\min}$). I have identified the form of the dependence on this parameter and roughly determined the constants $\alpha_1$ and $\alpha_2$ in Equation 4.8 to be of order unity. The results indicate that MR in graphene is governed by a classical transport mechanism described by mobility, carrier density and inhomogeneity density, rather than via a quantum effect. It is interesting to see that the inhomogeneity, which induces a large MR near Dirac point, has a significant remnant over a large range of carrier density, even to $n \gg n^*$, scaled by the inhomogeneity density $n^*$. Thus the results can serve as a basis for future detailed comparison between experiment and theory of charge inhomogeneity in this regime where there are few other experimental signatures.

Lastly I note that the extremely linear MR near the Dirac point in the most inhomogeneous Sample 3 remains a possible outlier to the universal description of MR developed here. Without a detailed theory of the MR it is impossible to say whether the linear MR can be explained within the classical framework using effective medium theory, or whether it points to new physics. I also note that a detailed description of the mechanism for producing inhomogeneity from the graphitic impurities is also lacking. Differences in the Raman 2D peak could be interpreted as changes in the electron dispersion (Fermi velocity) in impurity-decorated graphene due to band structure changes or changes in electron-electron interaction. It remains

to be seen whether the relevant inhomogeneity is in the electronic dispersion or in the scattering potential. Future scanned-probe studies may elucidate this. Moreover, the MR at low carrier density can not even be understood with effective medium theory since graphene p-n junctions play important role. Further theoretical and experimental investigations are called for to explain MR in this regime.

# Appendix A

## RAMAN SPECTROSCOPY OF GRAPHENE

The Raman effect describes inelastic scattering of light by the excitations of a solid such as phonons[81]. Thus Raman spectroscopy can be used to gain information about phonons and thus the crystal structure of graphene, by measuring the frequency, or energy, and strength of the quantum excitation in the Raman effect.

Figure A.1 shows a typical Raman spectrum of monolayer graphene. Raman intensity is enhanced when the incident and/or scattered light is resonant or nearly resonant with an electronic transistion. In graphene, this electronic resonance condition leads to three important characteristic peaks of graphene: the D peak, the G peak and the 2D peak[29]. The G peak and D peak are first-order modes of the Raman effect where the incident and scattered light are resonant with transitions in one valley. The G peak thus results from excitation of phonon near zero momentum. The line width of the G peak is mainly due to the anharmonicity of the optical phonon. The D peak corresponds to zone-edge phonons and is a result of the breaking-down of momentum conservation, a sign of disorder in a graphene sample. The 2D peak arises from a second-order Raman process involving scattering of an excited electron and a hole from one valley to another via two zone-edges, the so called inter-valley transition. The 2D peak is entirely resonant and does not require disorder.

A pristine monolayer graphene usually shows characteristic sharp G and 2D peak which are Lorentzian in lineshape, and a suppressed or absent D peak. The 2D peak of multi-layer graphene is broader and consists of multiple Lorentzian peaks: four peaks, for example, for bi-layer graphene. This is the result of multiple 2D subbands in multi-layer graphene, resulting in multiple resonance conditions. The relative intensity of the 2D to the G peak is usually close to 2. For mono-layer graphene synthesized via CVD, the above rules may be violated[21, 35], except for the Lorentzian lineshape of the 2D peak. As the layer-number increases, the number of possible modes contributing to the 2D peak increases dramatically, making the discrimination between different layer numbers difficult. Besides, as an optical technique, the resolution of Raman spectroscopy is limited by optical wavelengths and is not suitable for examining graphene's structure on the nanometers scale.

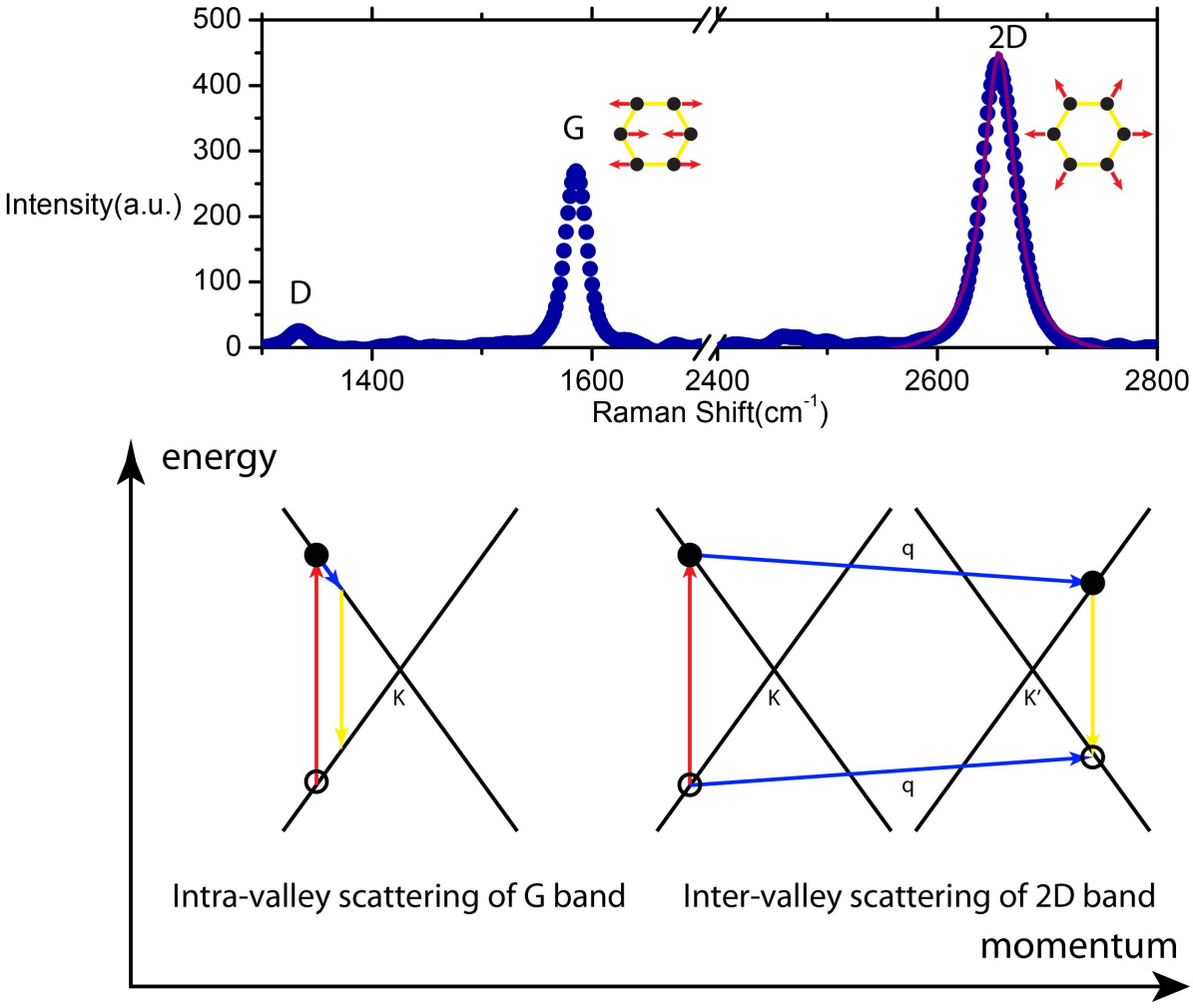


Figure A.1: The D, G and 2D peaks of a typical Raman spectrum of graphene. The pink curve is the Lorentzian fit for the 2D peak. The oscillation of the atoms for the G and 2D peaks are shown beside the corresponding peaks. A schematic of the resonance process for the G peak and 2D peak is shown below. Optical phonons are generated during the process of the incidence(red) and emission(yellow) of photons; for the G peak (left) a single phonon near $q = 0$ is excited, and for the 2D peak (right) two phonons with $q \approx K$ are excited. Electrons and holes are denoted by solid and hollow circles.

# Appendix B

## BOLTZMANN MAGNETO-TRANSPORT APPROACH

In this Appendix we deduce the non-magnetoresistance of a single-carrier conductor and the quadratic magnetoresistance of a two-carrier conductor from Boltzmann's transport equation based on Ziman's *Theory of Solids*[82].

In a steady(but not the equilibrium) state,

$$\frac{\partial f_{\mathbf{k}}}{\partial t}\Big]_{\text{diff.}} + \frac{\partial f_{\mathbf{k}}}{\partial t}\Big]_{\text{field}} + \frac{\partial f_{\mathbf{k}}}{\partial t}\Big]_{\text{scatt.}} = 0, \tag{B.1}$$

where $f_{\mathbf{k}}$ is the number of carriers in the neighbourhood of $\mathbf{r}$ at time $t$. The rate of change of the distribution due to diffusion is

$$\frac{\partial f_{\mathbf{k}}}{\partial t}\Big]_{\text{diff.}} = -\mathbf{v}_{\mathbf{k}} \cdot \frac{\partial f_{\mathbf{k}}}{\partial \mathbf{r}}. \tag{B.2}$$

(i) By writing

$$g_{\mathbf{k}} = f_{\mathbf{k}} - f^0_{\mathbf{k}}, \tag{B.3}$$

in which $f^0_{\mathbf{k}}$ is the equilibrium Fermi distribution:

$$f^0_{\mathbf{k}} = \frac{1}{\exp\left[(\epsilon_{\mathbf{k}} - \mu)/k_{\text{B}}T\right]}, \tag{B.4}$$

where $\epsilon_{\mathbf{k}}$ is the energy, $\mu$ is the chemical potential, $k_{\text{B}}$ is the Boltzmann constant and $T$ is the temperature, we have

$$\frac{\partial f_{\mathbf{k}}}{\partial t}\Big]_{\text{diff.}} = -\mathbf{v}_{\mathbf{k}} \cdot \frac{\partial f^0_{\mathbf{k}}}{\partial T}\nabla T - \mathbf{v}_{\mathbf{k}} \cdot \frac{\partial g_{\mathbf{k}}}{\partial \mathbf{r}}. \tag{B.5}$$

(ii) We write the term caused by the external field in Equation B.1 as

$$\frac{\partial f_{\mathbf{k}}}{\partial t}\Big]_{\text{field}} = \frac{e}{\hbar}\left(\mathbf{E} + \mathbf{v}_{\mathbf{k}} \times \mathbf{B}\right) \cdot \frac{\partial f_{\mathbf{k}}}{\partial \mathbf{k}}, \tag{B.6}$$

where $\mathbf{E}$ and $\mathbf{B}$ are the electrical and magnetic field respectively.

(iii) The effect of scattering is complicated. By introducting a relaxation time $\tau$, we make the following assumption:

$$\frac{\partial f_{\mathbf{k}}}{\partial t}\Big]_{\text{scatt.}} = \frac{1}{\tau} g_{\mathbf{k}}. \tag{B.7}$$

Substituting Equation B.5,B.6,B.7 into Equation B.1, and assuming (a) no temperature dependence and (b) small field, we have

$$e\mathbf{E} \cdot \mathbf{v}_{\mathbf{k}} \left(-\frac{\partial f^0}{\partial \epsilon}\right) = \frac{g_{\mathbf{k}}}{\tau} + \frac{e}{\hbar}\mathbf{v}_{\mathbf{k}} \times \mathbf{B} \cdot \frac{\partial g_{\mathbf{k}}}{\partial \mathbf{k}}. \tag{B.8}$$

Now we will discuss the Hall effect based on the Boltzmann transport equation. With a free electron assumption, namely,

$$\hbar\mathbf{k} = m\mathbf{v}, \tag{B.9}$$

we may substitute into the Boltzmann quation B.8 to obtain

$$\mathbf{v} \cdot \mathbf{E} = \mathbf{v} \cdot \mathbf{A} + \mu\mathbf{v} \times \mathbf{B} \cdot \mathbf{A}, \tag{B.10}$$

where $\mu = \frac{e\tau}{m}$, by imposing a solution of the form

$$g_{\mathbf{k}} = \left(-\frac{\partial f^0}{\partial \epsilon}\right) \tau \mathbf{v}_{\mathbf{k}} \cdot \mathbf{A}. \tag{B.11}$$

Thus we have

$$\mathbf{E} = \mathbf{A} + \mu\mathbf{B} \times \mathbf{A}, \tag{B.12}$$

whose solution is

$$\mathbf{A} = \frac{\mathbf{E} - \mu\mathbf{B} \times \mathbf{E}}{1 + (\mu B)^2}, \tag{B.13}$$

by a claim of elementary geometry.

With Equation B.11, we have

$$\begin{aligned} \mathbf{J} &= 2 \int e\mathbf{v}_\mathbf{k} f_\mathbf{k} d\mathbf{k} \\ &= 2 \int e\mathbf{v}_\mathbf{k} g_\mathbf{k} d\mathbf{k} \\ &= 2 \int e^2 \tau \mathbf{v}_\mathbf{k} (\mathbf{v}_\mathbf{k} \cdot \mathbf{A}) \left( -\frac{\partial f^0}{\partial \epsilon} \right) d\mathbf{k} \end{aligned} \tag{B.14}$$

Following the same deduction, the electronic conductivity without a magnetic field can be written as:

$$\boldsymbol{\sigma}_0 = 2 \int e^2 \tau \mathbf{v}_\mathbf{k} \mathbf{v}_\mathbf{k} \left( -\frac{\partial f^0}{\partial \epsilon} \right) d\mathbf{k}. \tag{B.15}$$

We now have

$$\mathbf{J} = \boldsymbol{\sigma} \cdot \mathbf{A}. \tag{B.16}$$

Thus in the presence of magnetic field, the current follows the same expression as there is no magnetic field, except that the electric field $\mathbf{E}$ is replaced by $\mathbf{A}$, as we can see in Equation B.13, $\mathbf{A} = \mathbf{E}$ is $\mathbf{B} = 0$.

Replacing $\mathbf{A}$ by $\mathbf{J}$, we have

$$\begin{aligned} \mathbf{E} &= \frac{1}{\sigma_0}\mathbf{J} + \mu\mathbf{B} \times \frac{1}{\sigma_0}\mathbf{J} \\ &= \rho_0 \mathbf{J} + \alpha \mathbf{B} \times \mathbf{J}, \end{aligned} \tag{B.17}$$

where $\alpha = \mu\rho^{(0)}$. Along the current we have

$$E_\parallel = \rho^{(0)} J \tag{B.18}$$

which means that the resistance of the specimen in unaltered by the magnetic field, i.e. there is no magnetoresistance.

In the direction perpendicular to $\mathbf{J}$ on the same plane, we have

$$E_H = \mu\rho^{(0)} BJ. \tag{B.19}$$

This is the Hall effect, and we can define a Hall coefficient:

$$\begin{aligned} R &= \mu\rho^{(0)} \\ &= \frac{1}{ne}, \end{aligned} \tag{B.20}$$

yielding

$$E_H = RBJ. \tag{B.21}$$

For a material with two types of carriers, the equation for the first charge carrier is B.17, namely:

$$\mathbf{E} = \frac{1}{\sigma_1^{(0)}} + \alpha_1 \mathbf{B} \times \frac{1}{\sigma_1^{(0)}} \mathbf{J_1} \tag{B.22}$$

and similarly for the second carrier

$$\mathbf{E} = \frac{1}{\sigma_2^{(0)}} + \alpha_1 \mathbf{B} \times \frac{1}{\sigma_2^{(0)}} \mathbf{J_2}. \tag{B.23}$$

Since $\mathbf{J} = \mathbf{J_1} + \mathbf{J_2}$, we have

$$\mathbf{J} = \left( \frac{\sigma_1^{(0)}}{1 + \alpha_1^2 B^2} + \frac{\sigma_2^{(0)}}{1 + \alpha_2^2 B^2} \right) \mathbf{E} - \left( \frac{\sigma_1^{(0)} \alpha_1}{1 + \alpha_1^2 B^2} + \frac{\sigma_2^{(0)} \alpha_2}{1 + \alpha_2^2 B^2} \right) \mathbf{B} \times \mathbf{E}, \tag{B.24}$$

which finally gives the quadratic magnetoresistance as

$$\begin{aligned}
\rho - \rho_{(0)} &= \frac{\mathbf{J}\cdot\mathbf{E}}{J^2} \\
&= \frac{\frac{\sigma_1^{(0)}}{1+\alpha_1^2B^2} + \frac{\sigma_2^{(0)}}{1+\alpha_2^2B^2}}{\left(\frac{\sigma_1^{(0)}}{1+\alpha_1^2B^2} + \frac{\sigma_2^{(0)}}{1+\alpha_2^2B^2}\right)^2 + \left(\frac{\sigma_1^{(0)}\alpha_1 B}{1+\alpha_1^2B^2} + \frac{\sigma_2^{(0)}\alpha_2 B}{1+\alpha_2^2B^2}\right)^2} - \frac{1}{\sigma_1^{(0)}+\sigma_2^{(0)}} \\
&= \frac{\sigma_1^{(0)}\sigma_2^{(0)}}{\sigma_1^{(0)}+\sigma_2^{(0)}} \frac{(\alpha_1-\alpha_2)^2B^2}{(\sigma_1^{(0)}+\sigma_2^{(0)})^2 + B^2(\alpha_1\sigma_1^{(0)}+\alpha_2\sigma_1^{(0)})^2}.
\end{aligned} \tag{B.25}$$

# Bibliography


[1] C. Lee, X. Wei, J. W. Kysar, and J. Hone. Measurement of the elastic properties and intrinsic stength of monolayer graphene. *Science*, 321:385, 2008.

[2] S. V. Morozov, K. S. Novoselov, M. I. Katsnelson, F. Schedin, D. C. Elias, J. A. Jaszczk, and A. K. Geim. Giant intrinsic carrier mobilities in graphene and its bilayer. *Phys. Rev. Lett.*, 100:016602, 2008.

[3] A.B. Kuzmenko, E. van Heumen, F. Carbone, and D. van der Marel. Universal optical conductance of graphite. *Phys. Rev. Lett.*, 100:117401, 2008.

[4] K. S. Novoselov, A. K. Geim, S. V. Morozov, D. Jiang, Y. Zhang, S. V. Dubonos, I. V. Grigorieva, and A. A. Firsov. Electric field effect in atomically thin carbon films. *Science*, 306:666, 2004.

[5] L. Gao, W. Ren, H. Xu, L. Jin, Z. Wang, T. Ma, L.-P. Ma, Z. Zhang, Q. Fu, L.-M. Peng, X. Bao, and H.-M. Cheng. Repeated growth and bubbling transfer of graphene with millimetre-size single-crystal grains using platinum. *Nature Comm.*, 3:699, 2012.

[6] S. Cho and M. S. Fuhrer. Charge transport and inhomogeneity near the minimum conductivity point in graphene. *Phys. Rev. B*, 77:081402(R), 2008.

[7] K. S. Novoselov, E. McCann, S. V. Morozov, V. I. Fal'ko, M. I. Katsnelson, U. Zeitler, D. Jiang, F. Schedin, and A. K. Geim. Unconventional quantum hall effect and berry's phase of $2\pi$ in bilayer graphene. *Nature Phys.*, 2:177, 2006.

[8] C. H. Lui, Z. Li, Z. Chen, P. V. Klimov, L. E. Brus, and T. F. Heinz. image stacking order in few-layer graphene. *Nano Lett.*, 11:164, 2011.

[9] A. A. Avetisyan, B. Partoens, and F. M. Peeters. Stacking order dependent electric field tuning of the band gap in graphene multilayers. *Phys. Rev. B*, 81:115432, 2010.

[10] P. R. Wallace. The band theory of graphite. *Phys. Rev.*, 71:622, 1947.

[11] M. I. Katsnelson, K. S. Novoselov, and A. K. Geim. Chiral tunnelling and the klein paradox in graphene. *Nature Phys.*, 2(620), 2006.

[12] M. P. Marder. *Condensed matter physics*. WILEY, 2010.

[13] M. I. Katsnelson. *Graphene: Carbon in Two Dimensions*. Cambridge, 2012.

[14] I. Pletikosic, M. Kralj, P. Pervan, R. Brako, J. Coraux, A. T. N'Daye, C. Busse, and T. Michely. Dirac cones and minigaps for graphene on ir(111). *Phys. Rev. Lett.*, 102:056808, 2009.

[15] X. Li, W. Cai, J. An, S. Kim, J. Nah, D. Yang, R. Piner, A. Velamakanni, I. Jung, E. Tutuc, S. K. Banerjee, L. Colombo, and R. S. Ruoff. Large-area synthesis of high-quality and uniform graphene films on copper foils. *Science*, 324:1312, 2009.

[16] P. Sutter. How silicon leaves the scene. *Nature Matter.*, 8:171, 2009.

[17] S. Bhaviripudi, X. Jia, M. S. Dresselhaus, and J. Kong. Role of kinetic factors in chemical vapor deposition synthesis of uniform large area graphene using copper catalyst. *Nano Lett.*, 10:4128, 2010.

[18] I. Vlassiouk, M. Regmi, P. Fulvio, S. Dai, P. Datskos, G. Eres, and S. Smirnov. role of hydrogen in chemical vapor depostion growth of large single-crystal graphene. *ACS Nano*, 5:6069, 2011.

[19] M. Losurdo, M. M. Giangregorio, P. Capezzuto, and G. Bruno. Graphene cvd grwoth on copper and nickel: role of hydrogen in kinetics and structure. *Phys. Chem. Chem. Phys.*, 13:20836, 2011.

[20] S. Bae, H. Kim, Y. Lee, X. Xu, J. Park, Y. Zheng, J. Balakrishnan, T. Lei, H. R. Kim, Y. I. Song, Y.-J. Kim, K. S. Kim, B. Ozyilmaz, J.-H. Ahn, B. H. Hong, and S. Iijima. Roll-to-roll production of 30-inch graphene films for transparent electrodes. *Nature Nano.*, 5:574, 2010.

[21] D. R. Lenski and M. S. Fuhrer. raman and optical characterization of multilayer turbostratic graphene grown via chemical vapor deposition. *J. Appl. Phys.*, 110:013720, 2011.

[22] V. Kochat, A. N. Pal, E. S. Sneha, A. Sampathkumar, A. Gairola, S. A. Shivashankar, S. Raghavan, and A. Ghosh. High contrast imaging and thickness determination of graphene with in-column secondary electron miscroscopy. *J. Appl. Phys.*, 110:014315, 2011.

[23] M. Ishigami, J. H. Chen, W. G. Cullen, M. S. Fuhrer, and E. D. Williams. Atomic structure of graphene on silicon dioxide. *Nano Lett.*, 7(6):1643–1648, 2007.

[24] P. Plachinda, S. Rouvimov, and R. Solanki. Structure analysis of cvd graphene films based on hrtem contrast simulations. *Phys. Status Solidi A*, 208:2681, 2011.

[25] S. Horiuchi, T. Gotou, M. Fujiwara, R. Sotoaka, M. Hirata, K. Kimoto, T. Asaka, T. Yokosawa, Y. Matsui, K. Watanabe, and M. Sekita. Carbon nanofilm with a new structure and property. *Jpn. J. Appl. Phys.*, 42:L1073, 2003.

[26] P. Huang, C. S. Ruiz-Vargas, A. M. van der Zande, W. S. Whitney, M. P. Levendorf, J. W. Kevek, S. Garg, J. S. Alden, C. J. Hustedt, Y. Zhu, J. Park,

P. L. McEuen, and D. A. Muller. Grains and grain boundries in single-layer graphena atomic patchwork quilts. *Nature*, 469:389, 2011.

[27] K. Kim, Z. Lee, W. Regan, C. Kisielowski, M. F. Crommie, and A. Zettl. Grain boundary mapping in polycrystalline graphene. *ACS Nano*, 5:2142, 2011.

[28] J. C. Meyer, A. K. Geim, M. I. Katsnelson, K. S. Novoselov, T. J. Booth, and S. Roth. The structure of suspended graphene sheets. *Nature*, 446:60, 2007.

[29] A. C. Ferrari, J. C. Meyer, V. Scardaci, C. Casiraghi, M. Lazzeri, F. Mauri, S. Piscanec, D. Jiang, K. S. Novoselov, S. Roth, and A. K. Geim. Raman spectrum of graphene and graphene layers. *Phys. Rev. Lett.*, 97:187401, 2006.

[30] S. Lee, K. Lee, and Z. Zhong. Wafer scale homogeneous bilayer graphene films by chemical vapor deposition. *Nano Lett.*, 10:4702, 2010.

[31] J. Martin, N. Akerman, G. Ulbricht, T. Hohmann, J. H. Smet, K. von Klitzing, and A. Yacoby. Obersevation of electron-hole puddles in graphene using a scanning single-electron transistor. *Nature Phys.*, 4:144–148, 2007.

[32] Y. Zhang, V. W. Brar, C. Girit, A. Zettl, and M. F. Crommie. Origin of spatial charge inhomogeneity in graphene. *Nature Phys.*, 5:722–726, 2009.

[33] G. Li, A. Luican, J. M. B. Lopes dos Santos, A. H. Castro Neto, A. Reina, J. Kong, and E. Y. Andrei. Observation of van hove singularirities in twisted graphene layers. *Nature Phys.*, 6:109–113, 2010.

[34] L. Brown, R. Hovden, P. Huang, M. Wojcik, D. A. Muller, and J. Park. Twinning and twisting of tri- and bilayer graphene. *Nano Lett.*, 12:1609, 2012.

[35] J. Ping and M. S. Fuhrer. Layer number and stacking sequence imaging of few-layer graphene by transmission electron microscopy. *Nano Lett.*, 12:4635, 2012.

[36] D. B. Williams and C. B. Carter. *Transmission electron microscopy: a textbook for materials science*. Springer, 2009.

[37] R. F. Egerton. *Physical principles of electron microscopy*. Springer, 2005.

[38] M. M. J. Treacy. Z dependence of electron scattering by single atoms into annular dark-field detectors. *Microsc. Microanal.*, 17:847, 2011.

[39] B. Hu, H. Ago, Y. Ito, K. Kawahara, M. Tsuji, E. Magome, K. Sumitani, N. Mizuta, K. Ikeda, and S. Mizuno. Epitaxial growth of large-area single-laeyr graphen over cu(111)/sapphire by atomspheric pressure cvd. *Carbon*, 50:57–65, 2012.

[40] R. Chen and P. Trucano. Comparisons of atomic thermal motions for graphite at 300 k based on x-ray, neutron, and phonon-spctrum data. *Acta Cryst.*, A34:979, 1978.

[41] F. Banhart, J. Kotakoski, and A. V. Krasheninnikov. Structural defects in graphene. *ACS Nano*, 5:26, 2011.

[42] K. Huang and H. H. Wills. X-ray reflextions from dilute solid solutions. *Proc. R. Soc. Lond. A*, 190:102, 1947.

[43] M. M. Lucchese, F. Stavale, E. H. M. Ferreira, C. Vilani, M. V. O. Moutinho, R. B. Capaz, C. A. Achete, and A. Jorio. Quantifying ion-induced defects and raman relaxation length in graphene. *Carbon*, 48:1592, 2010.

[44] W. Zhang, P. Wu, Z. Li, and J. Yang. First-principles thermodynamics of graphene growth on cu surfaces. *J. Phys. Chem. C*, 115:11782–17787, 2011.

[45] H. Chen, W. Zhu, and Z. Zhang. Contrasting behavior of carbon nucleation in the initial stages of graphene epitaxial growth on stepped metal surfaces. *Phys. Rev. Lett.*, 104:186101, 2010.

[46] S. Nie, W. Wu, S. Xing, Q. Yu, J. Bao, S. Pei, and K. F. McCarty. Growth from below: bilayer graphene on copper by chemical vapor deposition. *New J. Phys.*, 14:093028, 2012.

[47] A. Umair and H. Raza. Controlled synthesis of bilayer graphene on nickel. *Nanoscale Res. Lett.*, 7(437), 2012.

[48] A. Dahal, R. Addou, P. Sutter, and M. Batzill. Graphene monolayer rotation on ni(111) facilitates bilayer graphene growth. *Appl. Phys. Lett.*, 100:241602, 2012.

[49] Y. Xue, B. Wu, Y. Guo, L. Huang, L. Jiang, J. Chen, D. Geng, Y. Liu, W. Hu, and G. Yu. Synthesis of large-area, few-layer graphene on iron foil by chemical vapor depostion. *Nano Res.*, 4:1208, 2011.

[50] A. Das, S. Pisana, B. Chakraborty, S. Piscanec, S. K. Saha, U. V. Waghmare, K. S. Novoselov, H. R. Krishnamurthy, A. K. Geim, A. C. Ferrari, and A. K. Sood. Monitoring dopants by raman scattering in an electrochemcially top-gated graphene transistor. *Nature Nano.*, 3:210, 2008.

[51] P. Poncharal, A. Ayari, T. Michel, and J.-L. Sauvajol. Raman spectra of misoriented bilayer graphene. *Phys. Rev. B*, 78:113407, 2008.

[52] H. Cao, Q. Yu, A. Jauregui, J. Tian, and W. Wu. Electronic transport in chemical vapor deposited graphene synthesized on cu: quantum hall effect and weak localization. *Appl. Phys. Lett.*, 96:122106, 2010.

[53] X. Du, I. Skachko, A. Barker, and E. Y. Andrei. Approaching ballistic transport in suspended graphene. *Nature Nano.*, 3:491, 2008.

[54] Supriyo Datta. *Electronic transport in mesoscopic systems*. Cambridge, 1995.

[55] J. Nickel. Magnetoresistance overview. Technical report, Hewlett Packard Computer Peripherals Laboratory, 1995.

[56] J. Hu and T. F. Rosenbaum. Classical and quantum routes to linear magnetoresistance. *Nature Matter.*, 7:697–700, 2008.

[57] A. A. Abrikosov. Quantum magnetoresistance. *Phys. Rev. B*, 58(5):2788–2794, 1998.

[58] A. A. Abrikosov. Quantum linear magnetoresistance. *Europhys. Lett.*, 49(6):789–793, 2000.

[59] T. Ando. Screening effect and impurity scattering in monolayer graphene. *J. Phys. Soc. Jpn*, 75(7):074716, 2006.

[60] N. M. R. Peres, J. M. B Lopes dos Santos, and T. Stauber. Phenomenological study of the electronic transport coefficicents of graphene. *Phys. Rev. B*, 76:073412, 2007.

[61] P.W. Anderson. Absence of diffusion in certain random lattices. *Phys. Rev.*, 109(5):1492–1505, 1957.

[62] S. Adam, E. H. Hwang, V. M. Galitski, and S. Das Sarma. A self-consistent theory for graphene transport. *Proc. Nat. Acad. Sci. U.S.A.*, 104:18392–18397, 2007.

[63] E. H. Hwang, S. Adam, and S. Das Sarma. Carrier transport in two-dimensional graphene layers. *Phys. Rev. Lett.*, 98:186806, 2007.

[64] J.-H. Chen, C. Jang, S. Adam, M. S. Fuhrer, E. D. Williams, and M. Ishigami. Charged-impurity scattering in graphene. *Nature Phys.*, 4:377–381, 2008.

[65] K. Nomura and A. H. MacDonald. Quantum transport of massless dirac fermions. *Phys. Rev. Lett.*, 98:076602, 2007.

[66] V. V. Cheianov and V. I. Fal'ko. Friedel oscillations, impurity scattering, and temperature dependence of resistivity in graphene. *Phys. Rev. Lett.*, 97:226801, 2006.

[67] M. Trushin and J. Schliemann. Minimum electrical and thermal conductivity of graphene: a quasiclassical approach. *Phys. Rev. Lett.*, 99:216602, 2007.

[68] C. Kittel. *Introduction to solid state physics*. WILEY, eighth edition, 2005.

[69] Y. Zhang, Y.-W. Tan, H. L. Stormer, and P. Kim. Experimental observation of the quantum hall effect and berry's phase in graphene. *Nature*, 438(10):201–204, 2005.

[70] Z. Jiang, Y. Zhang, Y.-W. Tan, H. L. Stormer, and P. Kim. Quantum hall effect in graphene. *Solid Stat. Comm.*, 143:14–19, 2007.

[71] K. S. Novoselov, A. K. Geim, S. V. Morozov, D. Jiang, M. I. Katsnelson, I. V. Grigorieva, S. V. Dubonos, and A. A. Firsov. Two-dimensional gas of massless dirac fermions in graphene. *Nature*, 438:197–200, 2005.

[72] D. E. Soule. Magnetic field dependence of the hall effect and magnetoresistance in graphite single crystals. *Phys. Rev.*, 112:698–707, 1958.

[73] Y. Zhang, J. P. Small, M. E. S. Amori, and P. Kim. Electric field modulation of galvanomagnetic properties of mesoscopic graphite. *Phys. Rev. Lett.*, 94:176803, 2005.

[74] H. Kempa, P. Esquinazi, and Y. Kopelevich. Integer quantum hall effect in graphite. *Solid Stat. Comm.*, 138:118–122, 2006.

[75] A. L. Friedman, J. L. Tedesco, P. M. Campbell, J. C. Culbertson, E. Aifer, F. K. Perkins, R. L. Myers-Ward, J. K. Hite, Jr. C. R. Eddy, G. G. Jernigan, and D. K. Gaskill. Quantum linear magnetoresistance in multilayer epitaxial graphene. *Nano Lett.*, 10:3962–3965, 2010.

[76] V. Guttal and D. Stroud. Model for a macroscopically disordered conductor with an exactly linear high-field magnetoresistance. *Phys. Rev. B*, 71:201304(R), 2005.

[77] J. Ping and M. S. Fuhrer. Carbon impurities on graphene synthesized by chemical vapor deposition on platinum. *arXiv:1304.5123v1*, 2013.

[78] W. Long Q.-F. Sun and J. Wang. Disorder-induced enhancement of transport through graphene p-n junctions. *Phys. Rev. Lett.*, 101:166806, 2008.

[79] E. McCann, K. Kechedzhi, V. I. Fal'ko, H. Suzuura, T. Ando, and B. L. Altshuler. Weak-localization magnetoresistance and valley symmetry in graphene. *Phys. Rev. Lett.*, 97:146805, 2006.

[80] Y. Zhao, P. Cadden-Zimansky, F. Ghahari, and P. Kim. Magnetoresistance measurements of graphene at the charge neutrality point. *Phys. Rev. Lett.*, 108:106804, 2012.

[81] J. J. Sakurai. *Modern Quantum Mechanics (Revised Edition)*. Addison Wesley, 1 edition, 1993.

[82] J. M. Ziman. *Principles of the theory of solids*. Cambridge, 1972.